



Principal-component Interferometric Modeling (PRIMO), an Algorithm for EHT Data. I. Reconstructing Images from Simulated EHT Observations

Lia Medeiros^{1,4}, Dimitrios Psaltis², Tod R. Lauer³, and Feryal Özel²

¹ School of Natural Sciences, Institute for Advanced Study, 1 Einstein Drive, Princeton, NJ 08540, USA

² Steward Observatory and Department of Astronomy, University of Arizona, 933 N. Cherry Ave., Tucson, AZ 85721, USA

³ NSF's National Optical Infrared Astronomy Research Laboratory, Tucson, AZ 85726, USA

Received 2022 August 1; revised 2022 December 7; accepted 2022 December 8; published 2023 February 3

Abstract

The sparse interferometric coverage of the Event Horizon Telescope (EHT) poses a significant challenge for both reconstruction and model fitting of black hole images. PRIMO is a new principal components analysis-based algorithm for image reconstruction that uses the results of high-fidelity general relativistic, magnetohydrodynamic simulations of low-luminosity accretion flows as a training set. This allows the reconstruction of images that are consistent with the interferometric data and that live in the space of images that is spanned by the simulations. PRIMO follows Monte Carlo Markov Chains to fit a linear combination of principal components derived from an ensemble of simulated images to interferometric data. We show that PRIMO can efficiently and accurately reconstruct synthetic EHT data sets for several simulated images, even when the simulation parameters are significantly different from those of the image ensemble that was used to generate the principal components. The resulting reconstructions achieve resolution that is consistent with the performance of the array and do not introduce significant biases in image features such as the diameter of the ring of emission.

Unified Astronomy Thesaurus concepts: Very long baseline interferometry (1769); Black hole physics (159); Astronomy image processing (2306); Interferometry (808); Principal component analysis (1944); Accretion (14)

1. Introduction

The Event Horizon Telescope (EHT) Collaboration recently imaged the supermassive black hole in the nearby giant elliptical galaxy M87 for the first time using submillimeter very long baseline interferometry (VLBI) observations (Event Horizon Telescope Collaboration et al. 2019a, 2019b, 2019c, 2019d, 2019e, 2019f). The first polarized images of the black hole in M87 were published a short time later and indicated a strong and ordered magnetic field in the vicinity of the black hole (Event Horizon Telescope Collaboration et al. 2021a, 2021b).

Reconstructing images of the M87 supermassive black hole was challenging. The 2017 observations included only five telescope locations, resulting in markedly sparse interferometric (*uv*-plane) coverage. This challenge was extensively addressed in the EHT papers and particularly in Event Horizon Telescope Collaboration et al. (2019d), which is mainly concerned with a detailed discussion of the image reconstruction techniques used. In brief, a variety of algorithms was employed and all were extensively tested with simulations and intercompared on the images recovered from the actual observations. Of necessity, each algorithm incorporated a variety of assumptions to address the incomplete *uv*-plane coverage, which in turn imply associated uncertainties in the images recovered. The aim of this diverse approach was to be conservative with the reconstructions and ensure that the major quantities of astrophysical interest that were recovered from the images were robust.

⁴ NSF Astronomy and Astrophysics Postdoctoral Fellow.

We begin with a discussion of the general image reconstruction techniques used so far, followed by the motivation for the PRIMO methodology that we introduce here.

General-purpose imaging algorithms: These include the traditional CLEAN algorithm (Högbom 1974), as well as new maximum likelihood methods (see, e.g., Chael et al. 2016; Akiyama et al. 2017; Event Horizon Telescope Collaboration et al. 2019d). The challenge for general-purpose image reconstruction algorithms is to generate an image among an infinite set of formally allowable solutions that are compatible with the data. In order to reduce the range of possible solutions, regularizers and secondary constraints (such as image global entropy, smoothness, local curvature, etc) are levied to recover an image that matches expectations of realistic structure. These methods are agnostic to theoretical predictions of image morphology and can therefore be used to determine basic image features such as the presence of a ring or brightness depression. However, introducing constraints on the plausibility of the image components is unavoidable and can lead to artifacts as shown, e.g., in Figure 10 of Event Horizon Telescope Collaboration et al. (2019d). Moreover, even though the regularizing conditions are reasonable for some astronomical images, they may not be well motivated for black hole images since simulations predict steep gradients in parts of the image (Psaltis et al. 2015).

Geometric fits: These are posterior sampling algorithms that fit semi-analytic or geometric crescent- and ring-like models directly to interferometric data (Kamruddin & Dexter 2013; Event Horizon Telescope Collaboration et al. 2019f). The models invoke a much smaller number of free parameters and therefore do not require additional regularizers the way that the general-purpose imaging algorithms do, as described above. However, in some cases these simple models may not be able to reproduce the complex image morphology predicted for black hole images. Indeed, simulations predict that the



Original content from this work may be used under the terms of the [Creative Commons Attribution 4.0 licence](#). Any further distribution of this work must maintain attribution to the author(s) and the title of the work, journal citation and DOI.

turbulent flows generate complex and stochastic structures as a consequence of the presence of bright, magnetically dominated flux tubes that are lensed by the black hole (see, e.g., Chan et al. 2015a; Event Horizon Telescope Collaboration et al. 2019e). Since the expected level of complexity is not included in the geometric model fits, the posteriors of the model parameters are affected by the most influential data points and may be biased (Psaltis et al. 2022).

Comparisons to numerical simulations: These methods compare simulated images from general relativistic magnetohydrodynamic (GRMHD) simulations to interferometric data, allowing for a rotation and scaling of the image relative to the data (see, e.g., Event Horizon Telescope Collaboration et al. 2019e). This comparison leads to constraints on physically meaningful parameters about the accretion flow. However, a single EHT observation corresponds to a particular realization of the turbulent structure of the accretion that may be consistent with simulations only in a statistical sense. As a consequence, these methods benefit from prior characterization of the statistics of the various image structures and of the corresponding interferometric observables (Kim et al. 2016; Event Horizon Telescope Collaboration et al. 2019f).

We present a novel principal-component interferometric modeling (PRIMO) algorithm that combines the desirable characteristics of the methods listed above while attempting to reduce their limitations. PRIMO uses a large library of GRMHD simulations as a “training set” for image reconstruction and model fitting. Instead of employing images that are smooth (as in the case of the maximum likelihood imaging methods) or consist of a limited number of broadened point sources (as in the case of CLEAN), it utilizes images that are broadly consistent with the space of possibilities spanned by the simulations. Because it involves a relatively small number of parameters, i.e., the coefficients of the principal components, it does not require imposing regularizers as is done in maximum likelihood methods. Furthermore, it is not limited to simple geometric shapes, such as crescents and rings, and can accurately reconstruct the stochastic features expected in black hole images. At the same time, it does not compare specific realizations of the turbulent images with the data but rather uses a principal-component decomposition to derive a basis for the space of possible images that are consistent with theoretical expectations. Finally, the principal components analysis (PCA) algorithm provides not only the best-fit image but rather a complete posterior over all image structures that are consistent with the data.

In addition to PCA, several other decompositions have been developed and applied to a multitude of problems. Using bases (called dictionaries), derived from PCA or other decompositions, to sparsely represent a training set falls under that umbrella of dictionary learning (see, e.g., Shao et al. 2014 for a review of dictionary learning applied to image denoising). Within astronomy, dictionary learning is frequently used to denoise images and spectra, or for image classification. Convolutional neural networks are also becoming ubiquitous in astronomy and have recently been applied to the output of the Clean algorithm to denoise the results of image reconstructions (Gheller & Vazza 2022). Our goal is not denoising in the image domain; PRIMO reconstructs images directly from the Fourier-domain visibilities. PCA is well suited for our application since it enables remarkably powerful dimensionality reduction, allowing us to fit only 20 PCA

components to the visibilities. Nonnegative matrix factorization, for example, is also commonly used in astronomical applications (see, e.g., Zhu 2016). However, requiring that the basis functions be positive definite can result in biases if the basis is truncated, especially near steep gradients like those expected near the boundary of the black hole shadow.

The PCA approach is very general but employs its own restrictions on the subset of allowable images by only requiring that the solution is likely to fall within the span of image morphologies produced by the training set of simulations. However, as is well known (see, e.g., Turk & Pentland 1991) and we will also demonstrate later, the PCA-based algorithm can reconstruct images even if the particular image structures are different in their details from the individual simulation snapshots that were used for the training set. Therefore, the method can be applied to reconstruct a black hole image even if the GRMHD outputs do not precisely represent all of its characteristics.

In Medeiros et al. (2018b), we showed that PCA could be used to efficiently represent the “space” of image morphologies seen in GRMHD simulations of an accreting black hole. The full range of structures seen in a simulation can then be encoded as a linear combination of a compact set of orthogonal “eigenimages,” with each eigenimage describing a portion of the structure seen in the simulation. Critically, PCA minimizes the number of components needed to describe the full variance of the simulation and the components can be ordered by the decreasing fraction of the variance that they describe.

A particular benefit of the PCA approach is that the orthogonal compact basis derived in image space transforms identically to the same basis that would be derived directly by representing the simulations in visibility (Fourier) space (see Medeiros et al. 2018b for a mathematical proof). In short, the basis can be built in the image domain, where we have the best a priori knowledge of the likely image morphology, but is fitted in the complementary visibility space in which the observations are presented.

Another benefit of PRIMO is that it not only provides excellent recovery of structure up to the formal resolution limit of the observations, but can provide “super-resolution” at yet finer scales. Rich knowledge of the intrinsic source structure allows for quantitative measures of features that could not be recovered without strong priors. The principal-component basis encodes the intrinsic correlations of the source structure over a range of angular scales. Interferometric observations of structure within the resolution limit can implicitly constrain the structure at finer angular scales somewhat beyond it.

Given a set of interferometric data and a compact set of eigenimages, the problem of image reconstruction and model fitting reduces to finding the relative weights of the eigenimages that are necessary for their weighted linear combination to be consistent with the data. It is important to emphasize, however, that while the image space of simulated images is completely sampled by the PCA basis, the EHT coverage provides only sparse, incomplete sampling of the visibility space. As such, the basis functions in that space (i.e., the visibility maps of the eigenimages) are no longer orthogonal when sampled only at the discrete EHT baselines. As a result, their coefficients must be fitted to the data with a procedure that respects the resultant covariances that now appear when the PCA components are fitted to the visibilities.

The goal of this paper is to progress from the initial presentation of the PCA image reconstruction methodology introduced by Medeiros et al. (2018b) to a complete description of how to apply it to analyzing the EHT observations of accreting supermassive black holes. In Section 2, we describe the GRMHD simulations that we used to construct the PCA basis, the preprocessing of the simulated images, and finally the PCA basis that we derived from them. In Section 3, we describe the Markov Chain Monte Carlo (MCMC) algorithm we use to fit interferometric data in order to obtain posteriors over the relative weights of the PCA components. We present results of applying PRIMO to simulated interferometric data in Section 4 and summarize our work in Section 5.

2. Building a PCA Basis from GRMHD simulations

As outlined in Medeiros et al. (2018b), we perform PCA on images generated from GRMHD simulations to describe the image space in which EHT images of real accreting black holes are likely to reside. In this section, we detail the methodology used to derive the linear combination of PCA components needed to fit a given data set.

2.1. The GRMHD Simulations

The GRMHD simulation images employed to generate the PCA basis were created using the massively parallel GPU-based code GRay (Chan et al. 2013). As input to the radiative transfer and ray-tracing simulations, we use two high-resolution GRMHD simulations with long time spans that were created using the 3D HARM code (Gammie et al. 2003; Narayan et al. 2012; Sadowski et al. 2013).

The configuration of a GRMHD simulation is specified by a set of physical parameters. For the purposes of validating our algorithm, we generated a set of 30 simulation runs, with parameters covering a wide range of possible emission models of the inner accretion flow around the black hole in M87, as follows.

1. GRMHD simulations only evolve the energy density of the plasma and therefore primarily the temperature of the ions and not of the electrons. In the accretion flow, the ion-to-electron temperature ratio is expected to be determined primarily by the plasma $\beta \equiv P_{\text{gas}}/P_{\text{mag}}$ parameter, which is the ratio of the local gas to magnetic pressures (Chan et al. 2015b). In the polar funnel, which is magnetically dominated, the two temperatures are expected to be nearly equal due to magnetic conduction (Ressler et al. 2015). In order to capture this behavior, we used a prescription for the electrons that sets the ion-to-electron temperature ratio T_i/T_e to (Mościbrodzka et al. 2016; Event Horizon Telescope Collaboration et al. 2019d)

$$\frac{T_i}{T_e} = R_{\text{high}} \frac{\beta^2}{1 + \beta^2} + \frac{1}{1 + \beta^2}. \quad (1)$$

We explore three values $R_{\text{high}} = 1, 20$, and 80 , but note that the simulations with $R_{\text{high}} = 1$ effectively result in an electron temperature that is equal to the ion temperature throughout the plasma, which is inconsistent with the assumption of a radiatively inefficient flow. We choose to include the simulations with $R_{\text{high}} = 1$ in our library only for consistency with previous EHT publications and in

order to explore a broad, albeit somewhat unphysical, range of image structures.

2. The electron density scale provides an overall normalization that sets the total accretion rate in the simulation. We explored values for the electron density scale of $n_e = 10^5, 2.5 \times 10^5, 5 \times 10^5, 7.5 \times 10^5$, and 10^6 cm^{-3} . We note that the higher values of electron number density are unlikely for M87, given the measured 1.3 mm flux and polarization signatures (Event Horizon Telescope Collaboration et al. 2019e, 2021b), but we include them in our simulation data set for completeness.
3. In half of the simulations, we used initial conditions that resulted in strong, ordered magnetic fields and a magnetically arrested disk (MAD, see, e.g., Narayan et al. 2012); in the other half, we used initial conditions that resulted in a less ordered, weaker, magnetic field, commonly referred to as standard and normal evolution (SANE, see, e.g., Igumenshchev et al. 2003).
4. We set the inclination angle of the black hole spin axis relative to the observer's line of sight to $i = 17^\circ$. This parameter only enters the radiative transfer calculation and determines the relative asymmetry of the image (see, e.g., Medeiros et al. 2022). We made this choice under the assumption that the spin axis of the black hole is parallel to the large-scale jet that has been observed at radio wavelengths (Walker et al. 2018). In the PCA model described below, we will allow for the possibility that the spin axis is either aligned or antialigned with the large-scale jet as well as for an arbitrary position angle of the spin axis in the plane of the sky. Even though the last two considerations affect the orientation of the black hole image in the sky, they are trivial geometric transformations and do not enter the GRMHD simulations.
5. We set the black hole mass to $M = 6.5 \times 10^9 M_\odot$ for the initial preparation of the simulations, which is a value consistent with the one obtained by stellar dynamics (Gebhardt et al. 2011) and by the first EHT imaging results (Event Horizon Telescope Collaboration et al. 2019f). Changing this value has two effects on the resulting simulations. First, it rescales the linear size of each image by a factor proportional to the mass. Second, it affects the outcome of the radiative transfer calculations by altering the synchrotron emission/absorption coefficients and by rescaling the photon path lengths. For the former effect, which is a trivial geometric transformation, we explore different mass values by rescaling the angular size of the PCA basis. For the latter effect, we note that, in the relevant range of parameters, the black hole mass is nearly degenerate with the electron number density scale n_e , with the image brightness at each pixel scaling as $\sim n_e^2 M$ (see Appendix A of Satapathy et al. 2022; see also Chan et al. 2015b). By exploring a broad range of values for the electron density scale and allowing for a rescaling of the images, we effectively probe a broad range of black hole masses.
6. We assumed a single black hole spin parameter of $a = 0.9$ for simplicity since image morphology is only weakly dependent on spin (Event Horizon Telescope Collaboration et al. 2019e). Indeed, as we show in later sections, the same PCA basis can also be used to reconstruct images of black holes with other spins.

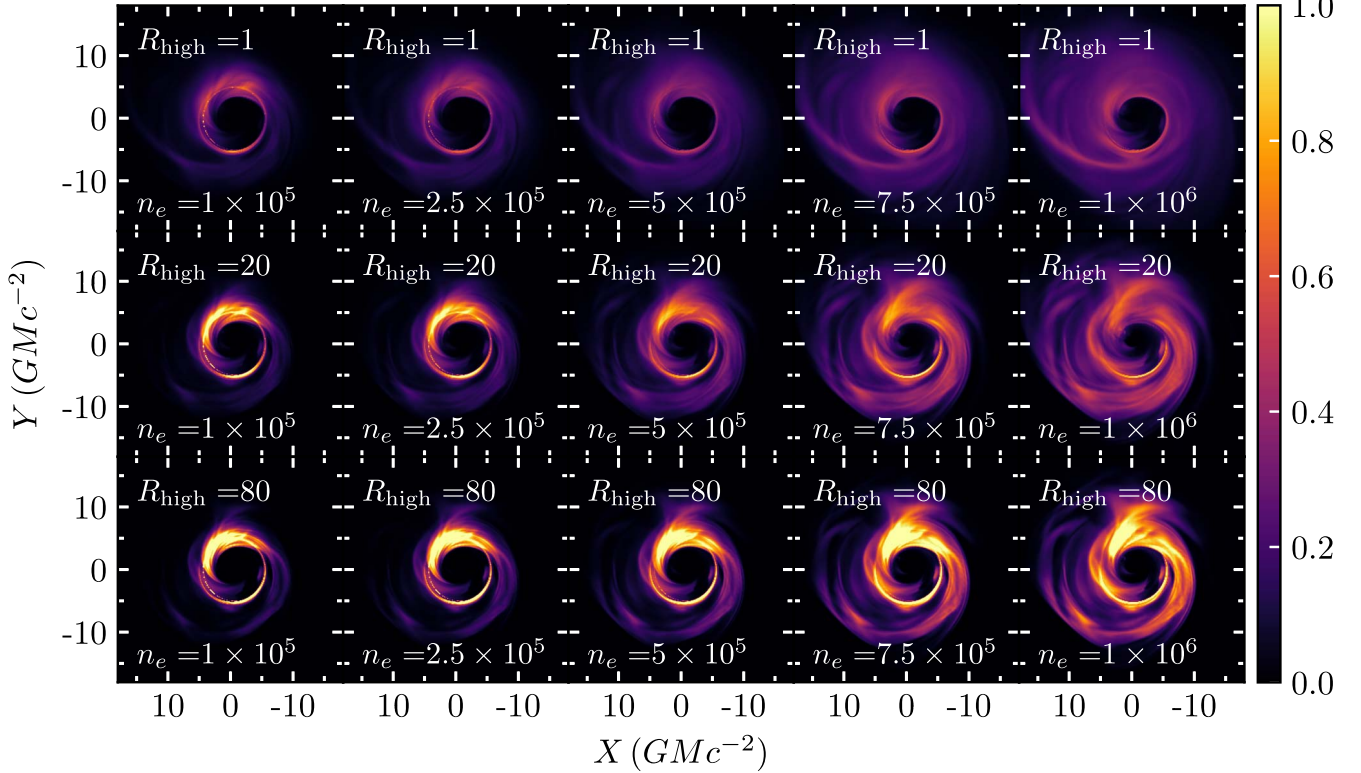


Figure 1. Effect of changing the electron density scale n_e (different columns) and the ion-to-electron temperature ratio R_{high} (different rows) on a single snapshot from a GRMHD simulation. This snapshot is from a MAD simulation with a black hole spin of $a = 0.9$ pointing upwards in each panel, with an observer inclination of $i = 17^\circ$ and a black hole mass of $M = 6.5 \times 10^9 M_\odot$. The brightness in each panel is normalized such that panels with the same value of n_e have the same total flux. Increasing the electron density scale leads to images with large ring widths whereas changing the temperature ratio alters the relative brightness of the accretion flow and funnel regions.

Figure 1 shows the effect of changing the electron number density scale, n_e , and the ion-to-electron temperature ratio R_{high} on a single snapshot from a MAD simulation. The electron number density scale affects primarily the width of the bright ring, with the latter increasing significantly with increasing n_e (Satapathy et al. 2022). In contrast, the temperature ratio R_{high} affects the relative brightness of different parts of the flow, altering the relative brightness between the funnel region and the accretion flow.

The set of parameters we discussed reflects a decision as to which sources of image variance to include in the PCA analysis and which parameters to treat externally. The position angle (ϕ) of the image on the sky, for example, can be included in our model trivially by an overall rotation of the PCA components and need not be included in the derivation of the components themselves. Whether the spin axis is pointing toward us at 17° or away from us at the complementary angle can also be incorporated in a similar manner, as it describes (statistically) a simple reflection. The effect of the black hole mass on image morphology is mostly degenerate with the electron density except for a change in the overall size of the image, which can be included trivially in the PCA model as a scaling of angular distances applied to all components. The overall source position is also not included in the PCA basis since the current set of EHT data only involve visibility amplitudes and closure phases, which are independent of the image location.

For each set of parameters, we generated 1024 image snapshots with a time resolution of $10 GM/c^3$. For the mass of M87, the time resolution equals ~ 3 days and 17 hours and each

simulation covers a total time span of over ten years. Each snapshot has a field of view of $64 GM/c^2$ and a resolution of $1/8 GM/c^2$ per pixel (approximately $0.5 \mu\text{as}$ resolution). Critically, the field of view is substantially larger than the measured size of the image, which is $\sim 10 GM/c^2$, and the resolution scale is sufficiently fine to avoid deleterious aliasing effects (Psaltis et al. 2020).

The set of 30 simulations provides a total of 30,720 images covering a broad range of image morphologies. Figure 2 shows several snapshots from a single simulation. Here we emphasize that although the parameters of the radiative transfer simulations can significantly affect gross image properties, such as the width of the ring of emission (see Figure 1), there is significant variance in image morphology even within a single simulation because of the stochastic nature of the MHD turbulence in the accretion flow (see also Medeiros et al. 2017, 2018a, 2018b).

2.2. Preparing the Simulated Images for PCA

The simulated images have significant structure at small scales, which the EHT cannot probe. Because we want the PCA basis to only reflect image variance on the physical scales observed by the EHT, we first need to eliminate the high-spatial-frequency structure in each simulated image.

To achieve this, we use a Butterworth filter (Butterworth 1930), which is effectively a low-pass filter, having a flat response for low Fourier frequencies and declining to zero smoothly at high frequencies. The Butterworth filter is defined

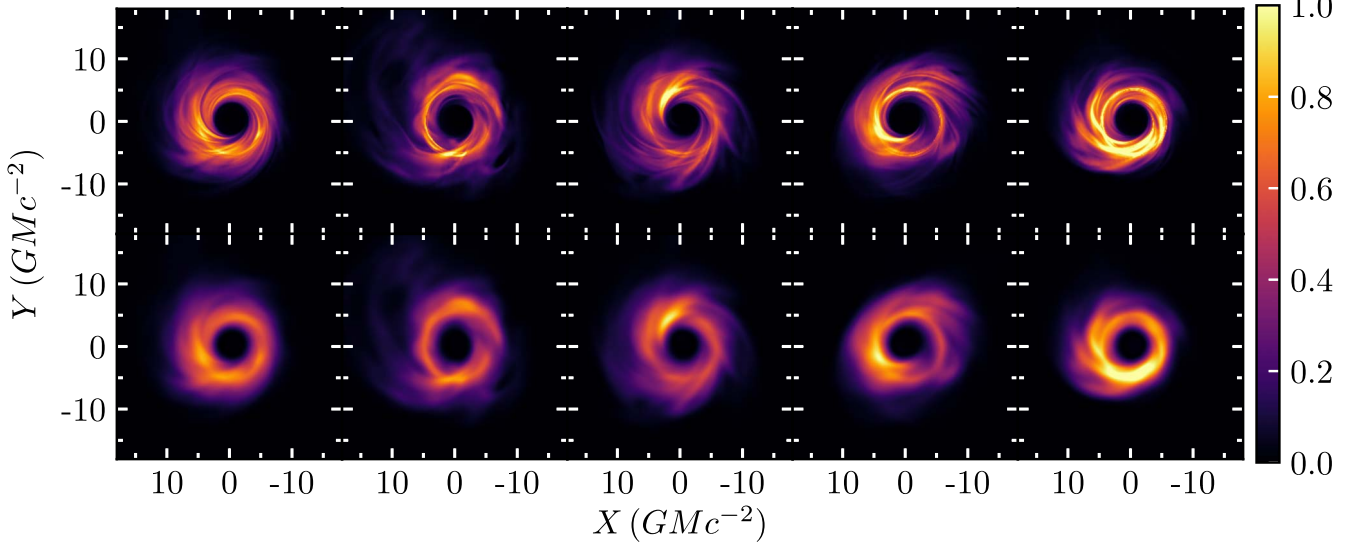


Figure 2. Top row: five representative snapshots from the MAD simulation with $n_e = 5 \times 10^5$, $R_{\text{high}} = 20$, $i = 17^\circ$, and $M = 6.5 \times 10^9 M_\odot$. Even within a single simulation, there is significant structural variability between the various snapshots. Bottom row: the same snapshots as the top row but filtered using a Butterworth filter with $n = 2$ and $r = 15 \text{ G}\lambda$, to mimic the finite resolution of the EHT. The brightness in each panel has been normalized such that all panels have the same total flux.

as

$$F_{\text{BW}}(b) = \left[1 + \left(\frac{b}{r} \right)^{2n} \right]^{-1/2}, \quad (2)$$

where r is the scale of the filter and n is a power-law index. We discuss in detail the motivation for using a Butterworth filter as well as the choice of parameters for EHT data analysis in Psaltis et al. (2020). The bottom row of Figure 2 shows the snapshots of the top row filtered by a Butterworth filter with $n = 2$ and $r = 15 \text{ G}\lambda$. This choice of filter parameters allows us to retain most of the power at baseline lengths probed by the EHT array, while filtering out most of the power at greater lengths.

As a second step, we normalize each filtered image to have the same total flux. Because images with higher electron density scale n_e have significantly higher total flux, not normalizing would have biased the PCA basis toward images with higher n_e values. We explored the effects of standardizing the images by their variance and found that this has a negligible effect on the PCA basis other than on the overall normalizations. We therefore do not standardize the images by their variance. We also do not mean-subtract the images before performing PCA, i.e., similar to what was done in Medeiros et al. (2018b), since the properties of the mean image are critical in fitting the observed data. If, instead, we had mean-subtracted the images before performing PCA, we would have needed to add back the mean image to the linear combination of PCA components, resulting in the same number of free parameters in the model.

Since all of the images correspond to the same black hole spin $a = 0.9$ and the same inclination angle $i = 17^\circ$, all of the black hole shadows are concentric and aligned with each other. For the case of M87, this is justified because of the known inclination of the large-scale jet as well as the weak dependence of the simulated images on black hole spin. If that were not the case, we would have also needed to recenter and align the

images before performing PCA, along the line of the approach in Medeiros et al. (2020).

2.3. Building the PCA Basis

Given the complete set of filtered simulated images, we generated the PCA basis following the procedures established in Medeiros et al. (2018b). Figure 3 shows the first 20 PCA components. The first PCA component is similar to the average image and contains a positive flux. The higher-order PCA components contain both positive and negative fluxes, since these components redistribute the flux present in the first component to approximate each individual snapshot.

The normalized eigenvalues corresponding to each PCA component are shown in the top left corner of each panel. Each eigenvalue measures the variance in pixel brightness of each PCA component, normalized such that the sum of all eigenvalues is equal to unity. Figure 4 shows the eigenvalue spectrum for this PCA decomposition. The first few PCA components account for the majority of brightness variance in the image and only 20 components are needed to account for 99% of the variance found in the full set of simulations. The slope of the eigenvalue spectrum for higher components is set by the power spectrum of the structures in the images (Medeiros et al. 2018b).

Figures 5 and 6 show the corresponding visibility amplitude and phase maps of the first 20 PCA components. It is a linear combination of these components in visibility space that we will fit directly to the data. As expected, the first few components contain primarily structures with low spatial frequencies (i.e., small baseline lengths) and describe primarily the broad-brush structure of the image. The remaining components contain significant power at high spatial frequencies (i.e., large baseline lengths) and describe the smaller structures in the image.

It is interesting that, although this was not explicitly imposed when performing the principal-component decomposition, components of increasing PCA order correspond to higher-order (m -fold) azimuthal symmetry. This is important when

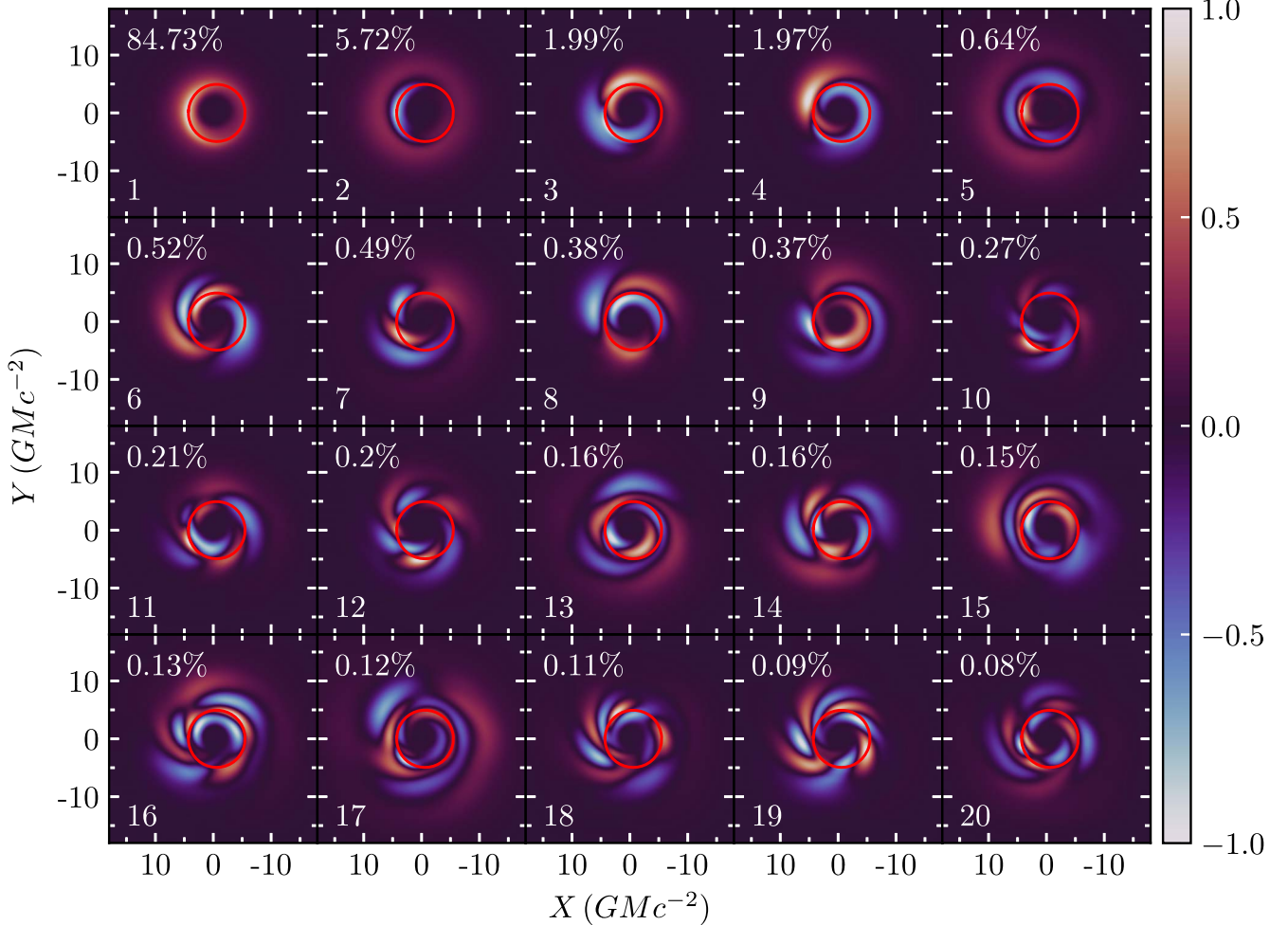


Figure 3. The first 20 PCA components for the set of simulated images employed in this paper. The respective proportions of variance explained are shown at the top left corner of each panel. Red closed curves show the analytically calculated size and shape of the black hole shadow boundary, defined as the critical impact parameter between photons that fall into the black hole and those that escape, as seen by an observer at infinity. The first PCA component is similar to the average image of the simulations, while contributions from the second component lead to thicker and thinner rings. The third and fourth components allow for either up–down or left–right asymmetries. The higher-order components describe smaller-scale structure indicative of the variance seen in the simulated snapshots. Each panel is normalized such that the full range of values falls within the range of the color bar.

comparing the angular structure of the PCA components to the locations of the EHT baselines for the 2017 M87 observations (Event Horizon Telescope Collaboration et al. 2019c), as also shown in Figures 5 and 6. Note that we have rotated the baseline tracks such that the black hole spin axis, which points upwards in all these panels, is at 288° east of north. Clearly, the first 20 PCA components already incorporate a substantial degree of azimuthal structure, which is finer than the angular separation of the dominant locations in visibility space probed by the EHT array. Lastly, note that each component comprises detail over a broad range of spatial frequencies. Within a given component, structural information on fine angular scales is correlated with that on broader scales. This allows visibilities within the EHT band limit to lead to inferences on the structure somewhat beyond it, producing reconstructions with a degree of “super-resolution.”

3. MCMC Algorithm

In order to fit EHT data, we implement the linear PCA model (PRIMO) into the MCMC algorithm Markov Chains for Horizons (MARCH, Psaltis et al. 2022). For the purposes of this initial exploration, we fit this model to synthetic EHT data

calculated for the baseline tracks of the array during the 2017 April 5 observations of M87.

3.1. The PCA Image Model

The PCA decomposition described in Section 2 allows us to construct a model for a black hole image that is a linear combination of N PCA components, with an appropriate rescaling, to account for a different black hole mass, and an appropriate rotation, to allow for different orientations in the sky.

We will be fitting data in the visibility domain and therefore we define the linear combination of the first N PCA components in that domain as

$$\tilde{I}(u, v) = \sum_{n=1}^N a_n \tilde{u}_n(u, v), \quad (3)$$

where \tilde{u}_n are the PCA components in the Fourier (u, v) domain, \tilde{I} is the Fourier-domain visibility of the reconstructed image, and a_n is the amplitude of the n th PCA component. Without loss of generality and in order to facilitate comparison with other astrophysical measurements of the source, we set $a_1 = 1$

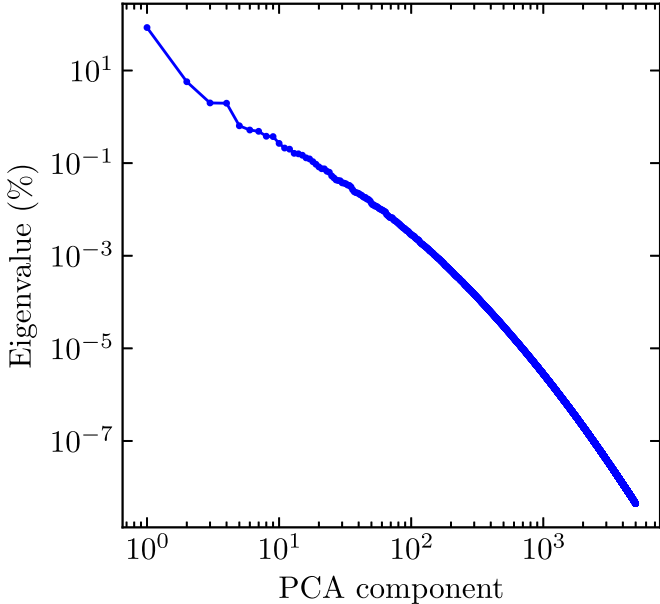


Figure 4. The spectrum of normalized eigenvalues for the first 5000 PCA components derived from a set of 30,720 GRMHD snapshots. Only 10 PCA components are necessary to reconstruct 98% of the total variance, whereas 20 can recover 99% of it.

and instead fit for the total zero-baseline visibility amplitude, which is also equal to the image flux

$$F = \sum_{n=1}^N a_n \tilde{\mathbf{u}}_n(0, 0). \quad (4)$$

By construction, this same linear combination of the PCA components in the image domain also generates the “best-fit” image, i.e.,

$$I(X, Y) = \sum_{n=1}^N a_n \mathbf{u}_n(X, Y), \quad (5)$$

where now I is the reconstructed image and \mathbf{u}_n are the PCA components, both in the image domain (X, Y).

In addition to the $N - 1$ PCA amplitudes and the flux normalization F , the model also includes three parameters that are implemented as a scaling, a rotation, and an up–down flip of the image. In particular, we introduce

1. A scaling parameter $\theta_g = GM/(Dc^2)$ that is applied to all PCA components in the sky domain (or equivalently θ_g^{-1} that is applied in the visibility domain). This scaling parameter quantifies the mass-to-distance ratio of the particular black hole we are modeling and allows us to convert the length scales in our images, which are in gravitational units, to angular sizes in the sky. This parameter can also be informed by the strong priors obtained by modeling the dynamics of stars around the black hole (Event Horizon Telescope Collaboration et al. 2019f).
2. A position angle ϕ , measured in degrees east of north, applied to all PCA components, that quantifies the orientation of the black hole spin on the plane of the sky.
3. A flip parameter $j = -1, 1$ that accounts for the possibility that the spin axis is pointing away from the observer and therefore that the accretion flow is rotating in a sense that is opposite to that of the simulation

(i.e., clockwise). In other words, if $j = -1$, we mirror all PCA components along the x -axis such that the rotation patterns will be oriented in the clockwise direction.

We note that, for computational efficiency, we do not use the three parameters θ_g , ϕ , and j to scale, rotate, and flip each of the PCA components. Instead, we use them to scale, rotate, and flip appropriately the small number of discrete u – v locations of the EHT baselines. We then calculate the linear sum of the PCA components at these locations using the interpolation technique we discuss below.

In total, the PCA model has $N + 3$ free parameters, where N is the number of PCA components used. Finally, it is worth emphasizing that, even though the PCA model is linear in most of its parameters, the visibility amplitudes and closure phases that we fit it to involve nonlinear operations.

3.2. Two-dimensional Interpolation

At each step of the MCMC chain, the algorithm calculates the model prediction at the (u, v) location of each data point and compares it to the data. Since the PCA image model is numerical and sampled on a regular array of pixels, we evaluate its prediction at any desired location using a 2D sinc interpolation, which has been demonstrated to cause no degradation of resolution of the 2D maps (Bracewell 1986). In 1D, a sinc function is defined as

$$\text{sinc}(u) = \frac{\sin(\pi u)}{\pi u}, \quad (6)$$

where u is the pixel coordinate in the Fourier domain. Interpolation in 2D is done with separable sinc kernels in u and v that are multiplied to form a 2D kernel.

Along each orientation, the value of the visibility at u' is given by

$$f(u') = \sum_n \frac{\sin[\pi(n - \Delta u)]}{\pi(n - \Delta u)} f(n), \quad (7)$$

where $f(n)$ is the image value at the integer n locations, and $\Delta u = u' - u$. In practice, we limit the kernel to a finite domain of $\pm u_0$, and taper it smoothly with a Gaussian to produce a well-behaved cutoff in the Fourier domain,

$$f(u') = \frac{1}{C_{\text{sinc}}} \sum_{n=-u_0/\Delta u}^{u_0/\Delta u} e^{-(n-\Delta u)^2/2\sigma^2} \frac{\sin[\pi(n - \Delta u)]}{\pi(n - \Delta u)} f(n), \quad (8)$$

where σ is chosen such that 2–3 cycles of the sinc function are included. The normalization constant C_{sinc} ensures that the interpolation kernel has an integral of unity, given the tapering and finite domain:

$$C_{\text{sinc}} = \sum_{n=-u_0/\Delta u}^{u_0/\Delta u} e^{-(n-\Delta u)^2/2\sigma^2} \frac{\sin[\pi(n - \Delta u)]}{\pi(n - \Delta u)}. \quad (9)$$

However, since the $\sin[\pi(n - \Delta u)]$ term is periodic with an amplitude specified by the Δu phase, its particular value, but for an alternating sign, is constant and thus is absorbed in the normalization. In practice, evaluating a trigonometric function

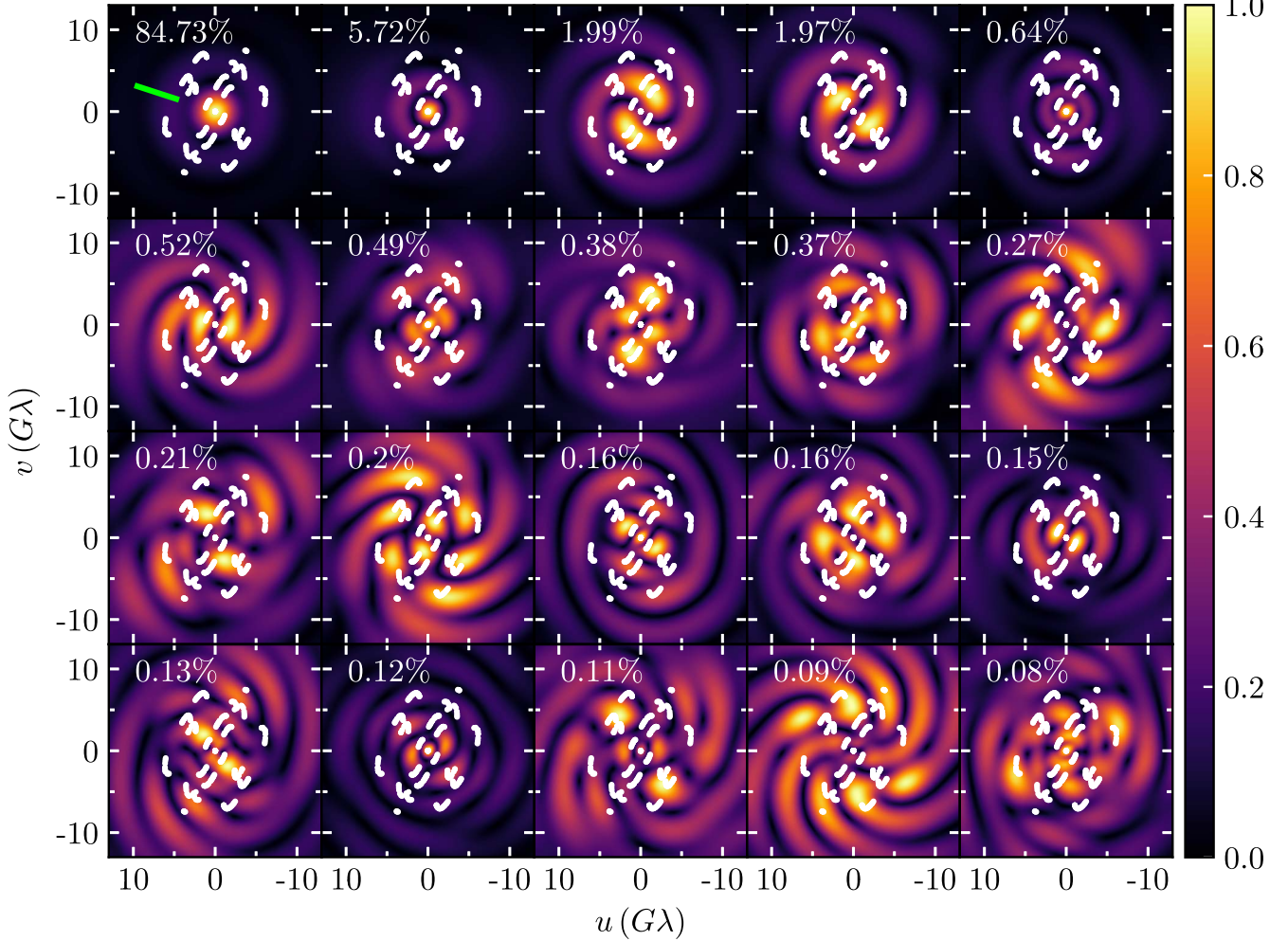


Figure 5. The visibility amplitude maps of the first 20 PCA components shown in Figure 3, normalized such that the peak in each component is equal to unity. The peak values in visibility amplitude for many of the components are offset from the center, indicating that there is significant negative flux in the images, as can be seen in Figure 3. White curves show the baseline tracks during the 2017 April EHT observations for the black hole in M87. In all panels, the black hole spin points upwards and the orientation of north is shown by the green line segment in the upper left panel.

is not required, since we can write

$$f(u') = \frac{1}{C'_{\text{sinc}}} \sum_{n=-u_0/\Delta u}^{u_0/\Delta u} \frac{e^{-(n-\Delta u)^2/2\sigma^2} (-1)^n}{n - \Delta u} f(u) \quad (10)$$

where

$$C'_{\text{sinc}} = \sum_{n=-u_0/\Delta u}^{u_0/\Delta u} \frac{e^{-(n-\Delta u)^2/2\sigma^2} (-1)^n}{n - \Delta u}. \quad (11)$$

3.3. The Posterior Distribution

Having defined a visibility-domain PCA model that depends on $N + 3$ model parameters, which we collectively denote by the vector $\vec{\theta}$, we use Bayes' theorem to write the posterior over these parameters as

$$P(\vec{\theta}|\text{data}) = C P_{\text{pri}}(\vec{\theta}) \mathcal{L}(\text{data}|\vec{\theta}). \quad (12)$$

Here, $P_{\text{pri}}(\vec{\theta})$ is the prior distribution over the model parameters, $\mathcal{L}(\text{data}|\vec{\theta})$ is the likelihood that the set of observations can be obtained from the model, and C is an appropriately defined normalization constant.

The set of data obtained by the EHT is a series of visibility amplitudes at the various baseline lengths between the different pairs of stations as well as a series of closure phases along all possible baseline triangles (Event Horizon Telescope Collaboration et al. 2019c). We calculate the likelihood function by multiplying the likelihoods of the individual visibility amplitude and closure phase data (see, however, Blackburn et al. 2019), assuming that all likelihoods are independent of each other:

$$\mathcal{L}(\text{data}|\vec{\theta}) = \prod_i \mathcal{L}_i(\text{data}|\vec{\theta}). \quad (13)$$

The precise definition of the various likelihoods is provided in detail in Psaltis et al. (2022). Because they depend only on the data products, they are the same for all models. The priors over the model parameters, however, are specific to each model, as we discuss in detail in the following subsection.

3.4. Priors

To ensure that our PCA model is probing physically relevant areas of the parameter space, we include a combination of

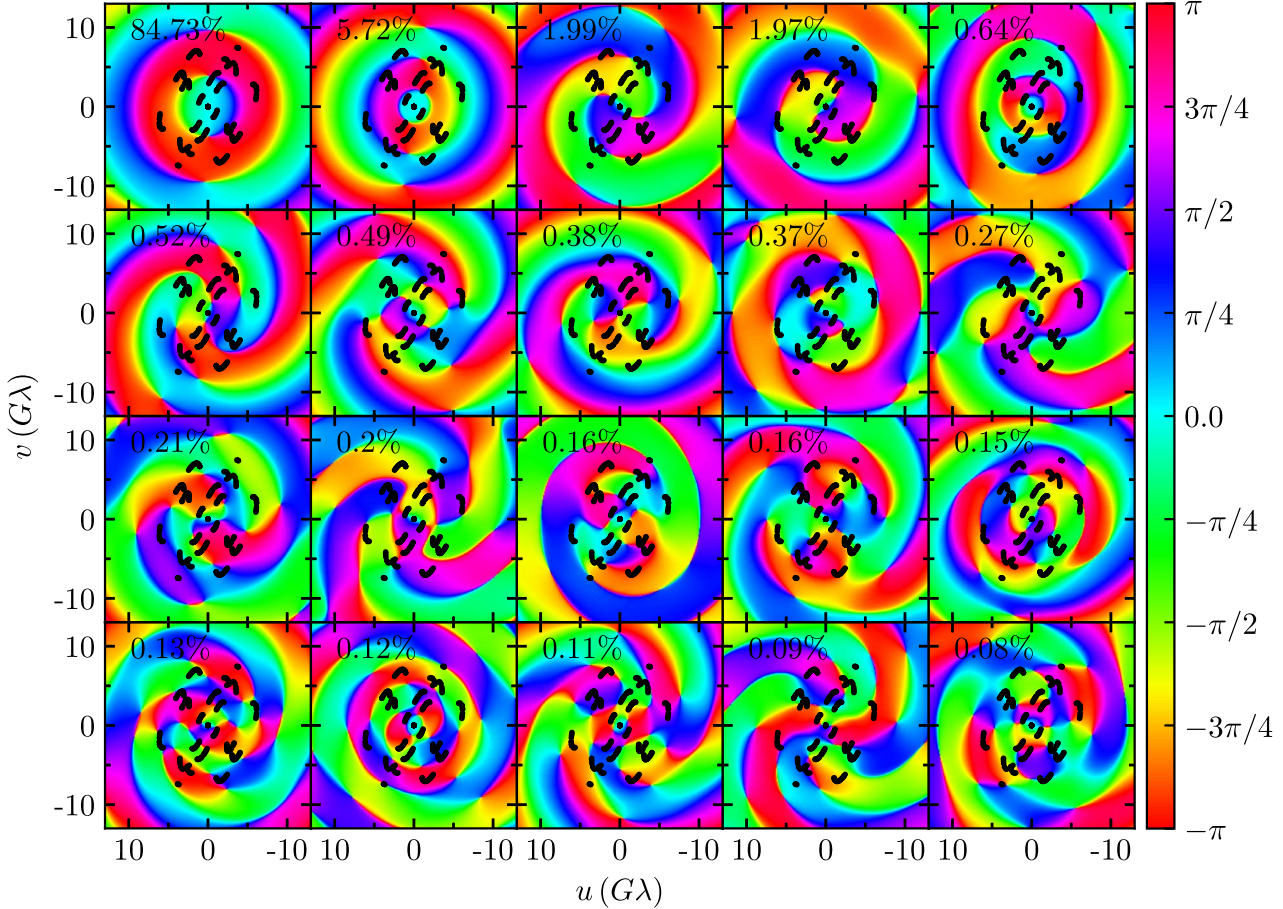


Figure 6. Same as Figure 5 but for visibility phase maps.

informative and uninformative priors on the various model parameters.

Because the EHT is an interferometer, the total flux F of the compact image cannot be directly measured without perfect knowledge of the prior calibration of the various telescope gains. However, it can often be independently constrained using other single-dish observations. Due to extended emission, the zero-baseline flux of the M87 EHT data was significantly higher than what was reasonably expected for the compact source (see the discussion in Appendix B of Event Horizon Telescope Collaboration et al. 2019d). Because of this, most M87 EHT analyses constrained the zero-baseline flux to a well-motivated value. To mirror those analyses, we fix the zero-baseline flux at 0.6 Jy, the value used to generate the synthetic data.

For the scaling parameter θ_g , there often exist prior measurements based on gas and/or stellar dynamics. For the M87 black hole, the two measurements are not statistically consistent with each other (see Gebhardt et al. 2011; Walsh et al. 2013). The envelope of the credible intervals for these two measurements is contained within the conservative range $1 \mu\text{as} \leq \theta_g \leq 6 \mu\text{as}$. For this reason, we simply use an uninformative prior

$$P(\theta_g) = \begin{cases} \theta_g^{-1} & \text{if } 1 \mu\text{as} \leq \theta_g \leq 6 \mu\text{as} \\ 0 & \text{otherwise.} \end{cases} \quad (14)$$

For the orientation parameter ϕ , we employ a highly informative prior based on the assumption that the black hole

spin is either aligned or antialigned with the large-scale jet observed at longer wavelengths, i.e., that

$$P(\phi) = \frac{1}{2\sqrt{2\pi\sigma_\phi^2}} [e^{-(\phi-\phi_0)^2/2\sigma_\phi^2} + e^{-(\phi-\phi_0+\pi)^2/2\sigma_\phi^2}]. \quad (15)$$

Here $\phi_0 = 288^\circ$ is the orientation of the large-scale jet (Walker et al. 2018). We set the widths of the two Gaussians to a nominal value of $\sigma_\phi = \pi/8$. We allow the flip parameter j to be equal to either 1 or -1 , with the same prior.

Finally, we employ informative priors on the amplitudes of the PCA components. Our aim is to give higher priors to images for which the amplitudes of the PCA components are not very dissimilar from the amplitudes that correspond to the simulated images used to calculate the PCA decomposition. However, we also do not wish to limit the fit to images that have precisely the same range of amplitudes as the training set. To achieve this, we first calculate the distribution of amplitudes for each PCA component found in the ensemble of training images and then broaden this distribution by a factor of two.

Figure 7 shows the distribution of normalized amplitudes, a_n/a_1 , for the PCA components 2 through 21 that we calculated above; note that, by definition, we have set $a_1 = 1$. Each panel also shows a Gaussian (in orange) with the same mean and standard deviation as the numerical distribution. These Gaussians provide good descriptions of the distributions for almost all of the components shown in the figure, with components 2 and 5 being notable exceptions. Both of these components contain structure that controls the width of the ring

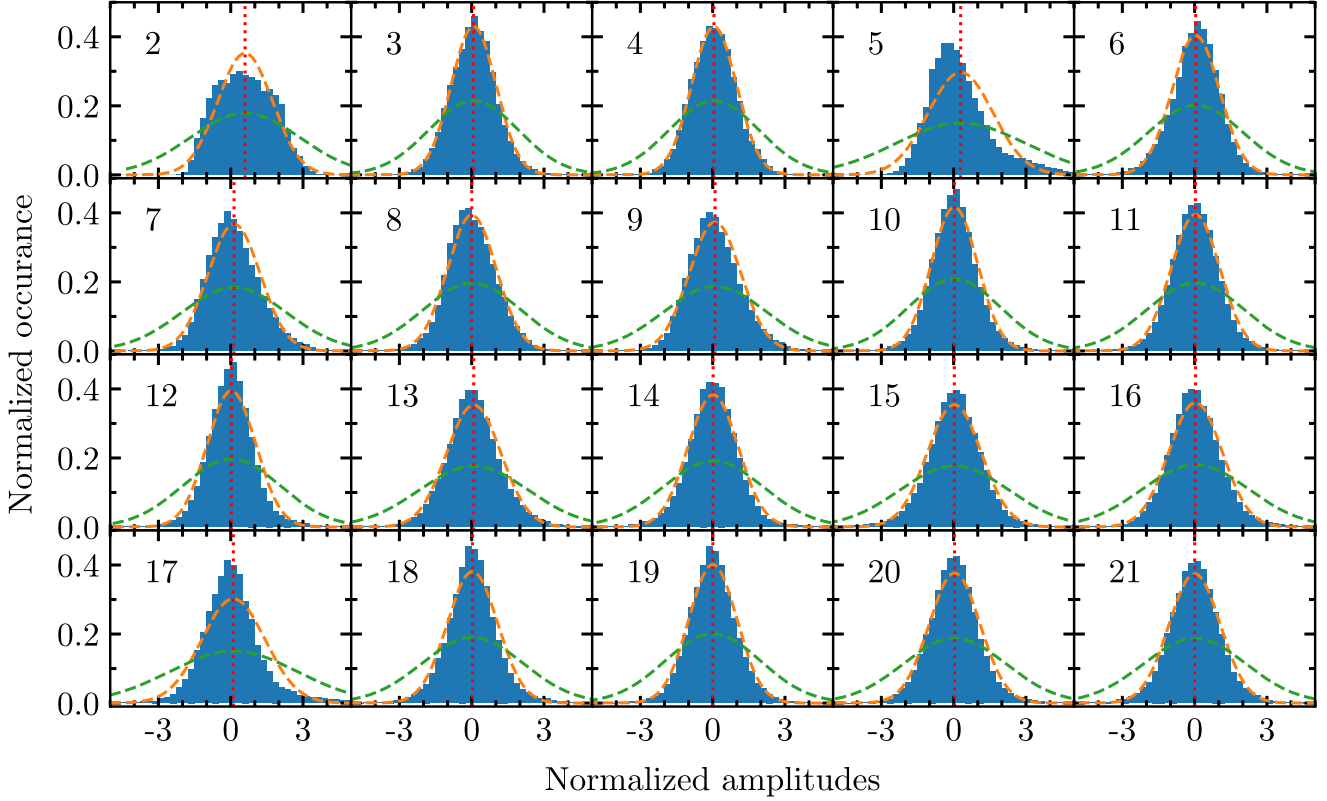


Figure 7. The distribution of the normalized amplitudes, a_n/a_1 , for PCA components 2 through 21. The red dotted lines show the mean of the distribution in each panel and the dashed orange lines show Gaussians with widths set by the standard deviations of the distributions and with peaks at the means of the distributions. The green dashed curves show the Gaussians broadened by a factor of two. We use the broadened Gaussians as priors to allow for reconstruction of images that are outliers within the distributions as well as of images that are similar to but are not contained in our training set.

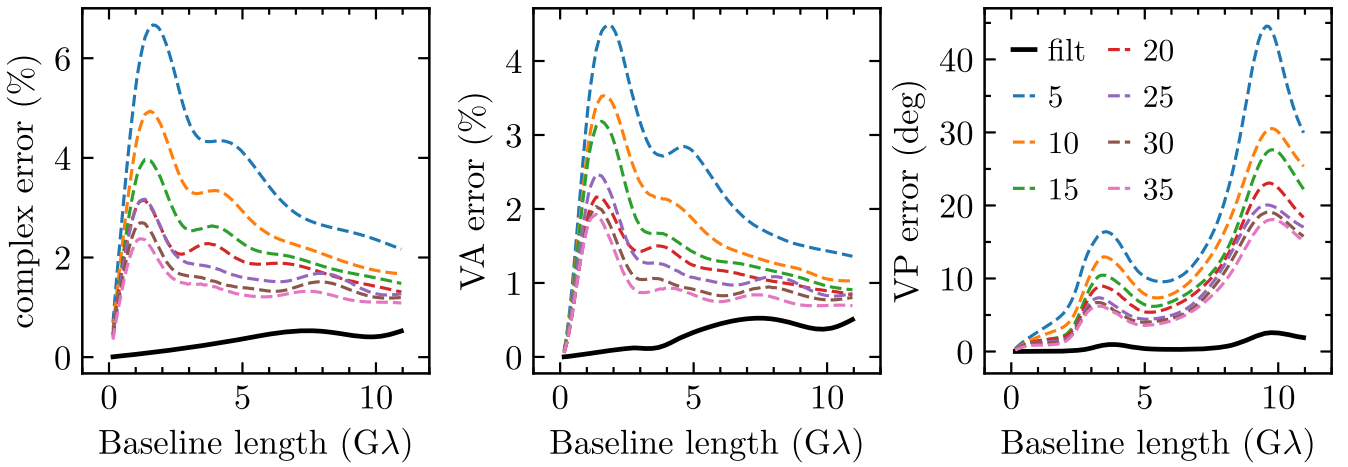


Figure 8. Fractional complex error ($\epsilon_{\text{complex}}$, left), fractional error in visibility amplitude (ϵ_{VA} , middle), and error in visibility phase (ϵ_{VP} , right) for reconstructions with 5, 10, 15, 20, 25, 30, and 35 PCA components. The black curve shows the error between the original unfiltered snapshot and the snapshot filtered with the Butterworth filter with $r = 15 \text{ G}\lambda$ and $n = 2$. All reconstructions are compared to the original unfiltered snapshot. We calculate these error quantities for each of the 30,720 snapshots, and then average them as a function of baseline length. The longest baseline that the 2017 EHT array could observe was $\sim 8 \text{ G}\lambda$. Reconstructions with 20 components achieve errors less than $\sim 3\%$ for $\epsilon_{\text{complex}}$, $\sim 2\%$ for ϵ_{VA} , and $\sim 15^\circ$ for ϵ_{VP} for baseline lengths observable by the 2017 EHT array.

in the image, which is strongly dependent on the simulation parameters (e.g., n_e). Therefore, the distributions of amplitudes for these components are not expected to follow a Gaussian distribution but rather will depend on the particular set of parameters used for the simulation library.

Gaussian distributions with the same mean but twice the standard deviation are also shown in each panel (green dashed lines) and comfortably include the full range of amplitudes

found in the training image set. In practice, for computational efficiency, we use these broadened Gaussians as priors on the amplitudes of each PCA component. In other words, we write the prior for the normalized amplitude of the n th PCA component a_n/a_1 as

$$P(a_n/a_1) = \left[e^{-\frac{1}{2} \left(\frac{a_n/a_1 - \bar{a}_n/a_1}{2\sigma_n} \right)^2} \right] / (\sqrt{2\pi} 2\sigma_n), \quad (16)$$

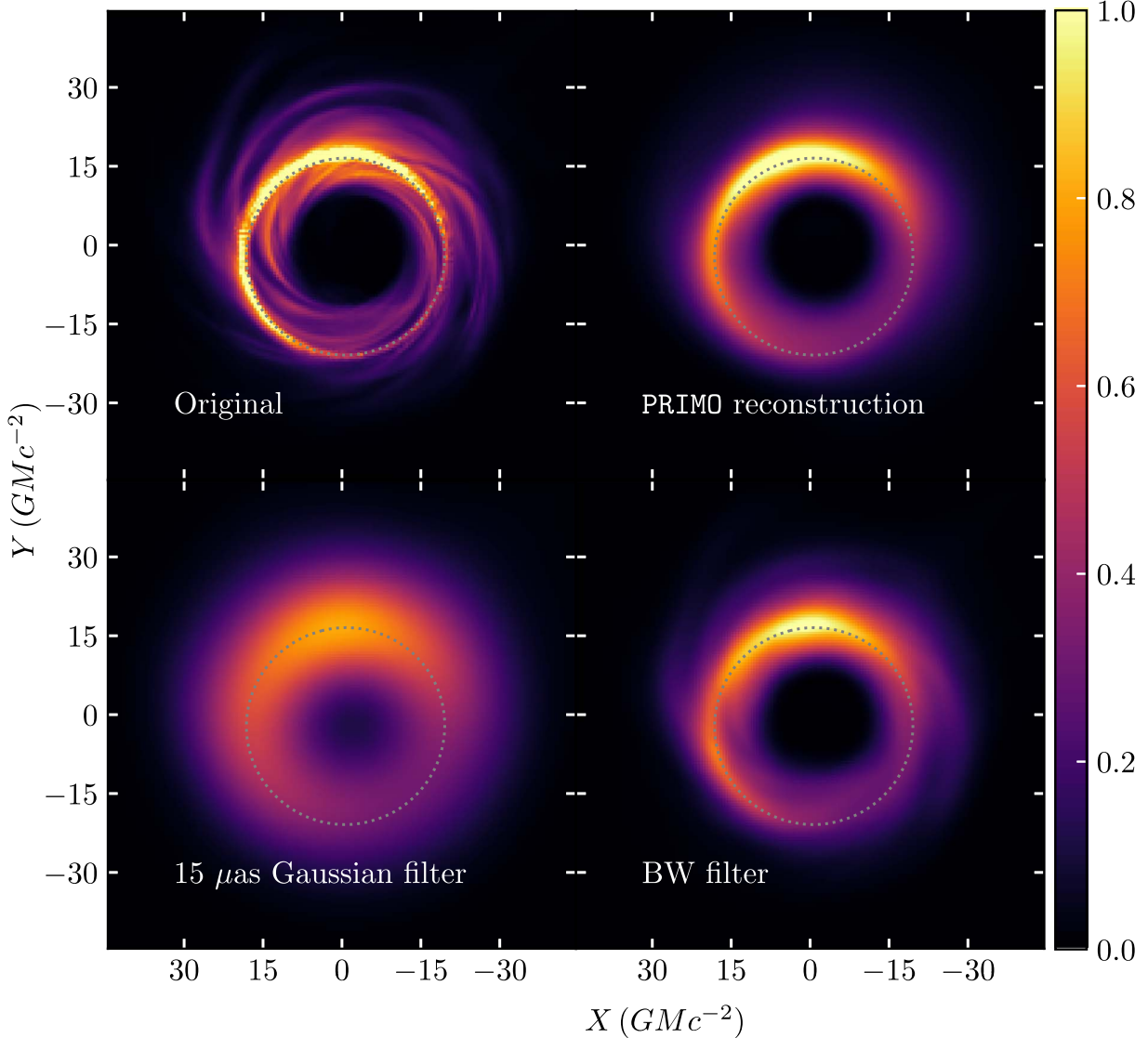


Figure 9. Top left: simulated image used for the generation of the first synthetic data set. Top right: the highest likelihood PRIMO reconstruction for the synthetic data. PRIMO can accurately reproduce the depth and shape of the brightness depression, the size and width of the ring of emission, and the brightness asymmetry of the ring. Bottom left: the original image blurred by a Gaussian filter with a width of $15 \mu\text{as}$, which mimics the nominal resolution of the EHT (see text). Bottom right: the simulated image convolved with a Butterworth filter with radius $r = 15 G\lambda$ and index $n = 2$. The brightness in all panels has been normalized such that all images have the same total flux, with the exception of the Gaussian-broadened image, which has a total flux that is 1.5 times higher than the other panels. In all panels, the gray dotted circles indicate the analytically calculated size and shape of the black hole shadow. The original and filtered images have been rotated to the position angle ϕ derived from the model.

where $\overline{a_n/a_1}$ and σ_n are the mean value and standard deviation of the distribution of normalized amplitudes of the training set.

3.5. Theoretical Uncertainty

In most applications of PCA, one can reconstruct an image by simply projecting the image onto the PCA components to find the relative amplitude of each component that will result in the best possible reconstruction. Using a higher number of components will invariably result in a higher-fidelity reconstruction. A lossless reconstruction can always be achieved using all of the PCA components, if the image is part of the original set that was used to calculate the PCA decomposition. In the present application, however, we do not have a full image onto which we can project the components; we instead have sparse $u-v$ coverage. Attempting to fit a large number of components to sparse interferometric data can result in

overfitting since there may be several possible linear combinations of components that fit the data. Therefore, there exists an optimal number of PCA components for which the highest-fidelity reconstruction can be achieved by fitting the sparse interferometric data while respecting the resolution of the array.

In order to determine this optimal number and assess the error introduced by the truncation, we quantify the error in the visibility amplitudes between a reconstruction with N components and the original, unfiltered image in the Fourier domain as

$$\epsilon_{\text{complex}} = \frac{\sqrt{|(V_0 - V_N)(V_0^* - V_N^*)|}}{F}, \quad (17)$$

where F is the total flux of the image, V_N are the complex visibilities of the reconstruction, vertical bars indicate magnitude, and the asterisk denotes complex conjugation. We define

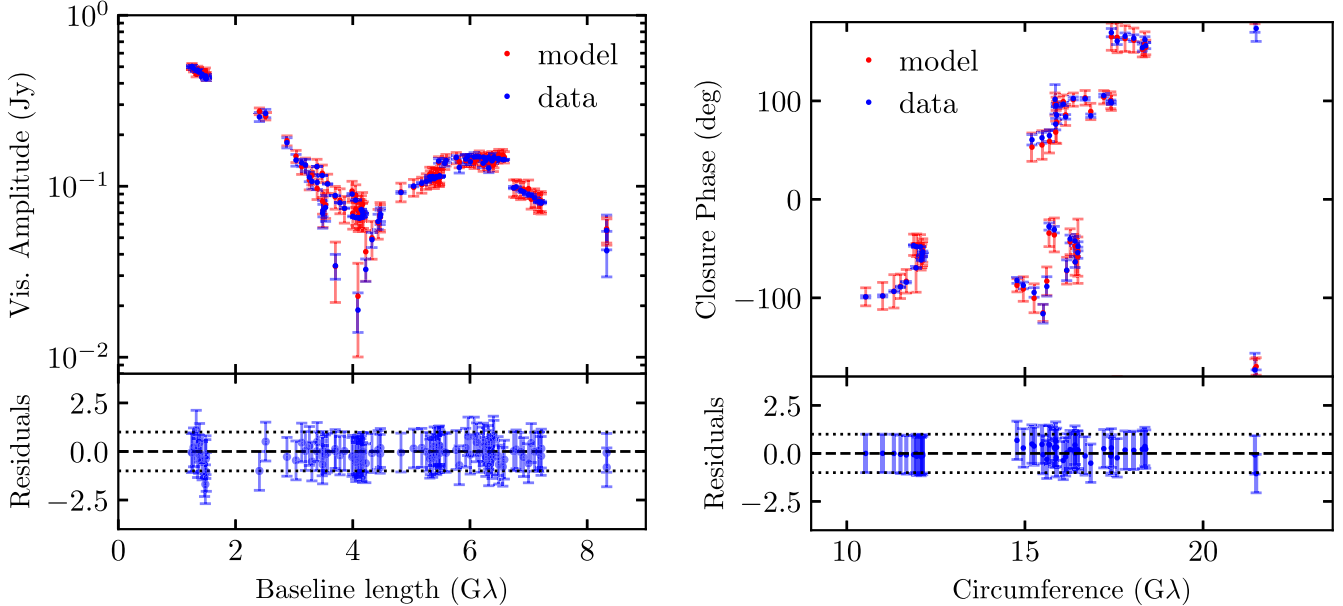


Figure 10. Left: synthetic visibility amplitude data and the amplitudes that correspond to the most likely PRIMO reconstruction. The theoretical uncertainty (see Section 3.5) is shown as error bars on the model. The residuals of the fit are shown below, with the theoretical and observational uncertainties having been added in quadrature. Right: the same but for the synthetic closure phase data.

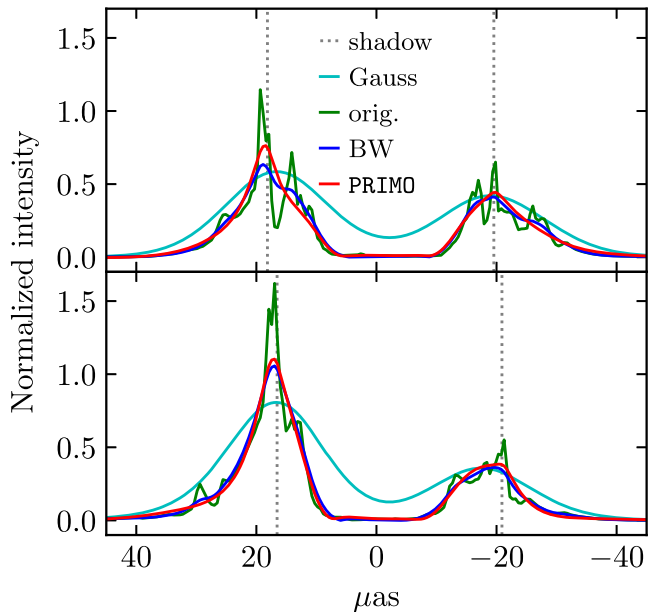


Figure 11. Comparison of the horizontal (top) and vertical (bottom) cross sections of the images shown in Figure 9. The curves show the original snapshot (green), the snapshot filtered with a Butterworth filter (blue), the most likely PRIMO reconstruction (red), the snapshot filtered with a 15 μ as Gaussian (cyan), and the analytically calculated edges of the black hole shadow (gray dotted vertical lines). The cross sections are normalized such that all images have the same total flux, except for the Gaussian-broadened image, which has 1.5 times the flux of the other images. The y-axis is in arbitrary units. PRIMO can accurately reproduce the main features of the image and does not introduce a significant bias in the ring size.

the fractional error in visibility amplitude as

$$\epsilon_{VA} = \left| \frac{|V_{\text{orig}}| - |V_{\text{recon}}|}{F} \right|, \quad (18)$$

where $|V_{\text{orig}}|$ and $|V_{\text{recon}}|$ denote the amplitude of the complex visibilities for the original and reconstructed images

respectively. The error in visibility phase is defined as

$$\epsilon_{VP} = |\arg(V_{\text{orig}}) - \arg(V_{\text{recon}})| \quad (19)$$

if this quantity is $< 180^\circ$ and

$$\epsilon_{VP} = 360^\circ - |\arg(V_{\text{orig}}) - \arg(V_{\text{recon}})| \quad (20)$$

otherwise. We calculate these errors for each baseline length by averaging along different azimuthal orientations and over the complete set of images in the training set.

In both equations above, $\arg(V)$ denotes the argument or phase of the complex visibilities of the images. When taking the average of the error in visibility phase, we follow Mardia & Jupp (2009) and define the average of a directional quantity as

$$\bar{\theta} = \begin{cases} \tan^{-1}(\bar{S}/\bar{C}), & \text{if } \bar{C} \geq 0 \\ \tan^{-1}(\bar{S}/\bar{C}) + \pi, & \text{if } \bar{C} < 0, \end{cases} \quad (21)$$

where

$$\bar{S} = \frac{1}{n} \sum_{j=1}^n \sin \theta_j \quad (22)$$

$$\bar{C} = \frac{1}{n} \sum_{j=1}^n \cos \theta_j.$$

Figure 8 shows the errors $\epsilon_{\text{complex}}$, ϵ_{VA} , and ϵ_{VP} as functions of baseline length, for all 30,720 snapshots and for different values of the number N of PCA components. The figure also compares these errors to those introduced to the original images by the application of the Butterworth filter. In all three error quantities, there are significant broad peaks at around 1–4 G λ , which are introduced by the dips, or nulls, that exist in the training set around these baseline lengths (see Medeiros et al. 2017 for a discussion of the origin of these uncertainties).

The longest baselines included in the 2017 EHT array are about 8 G λ . Reconstructions with 20 components achieve fractional complex errors less than $\sim 3\%$ at all baselines less than 8 G λ , even at baseline lengths that frequently have a

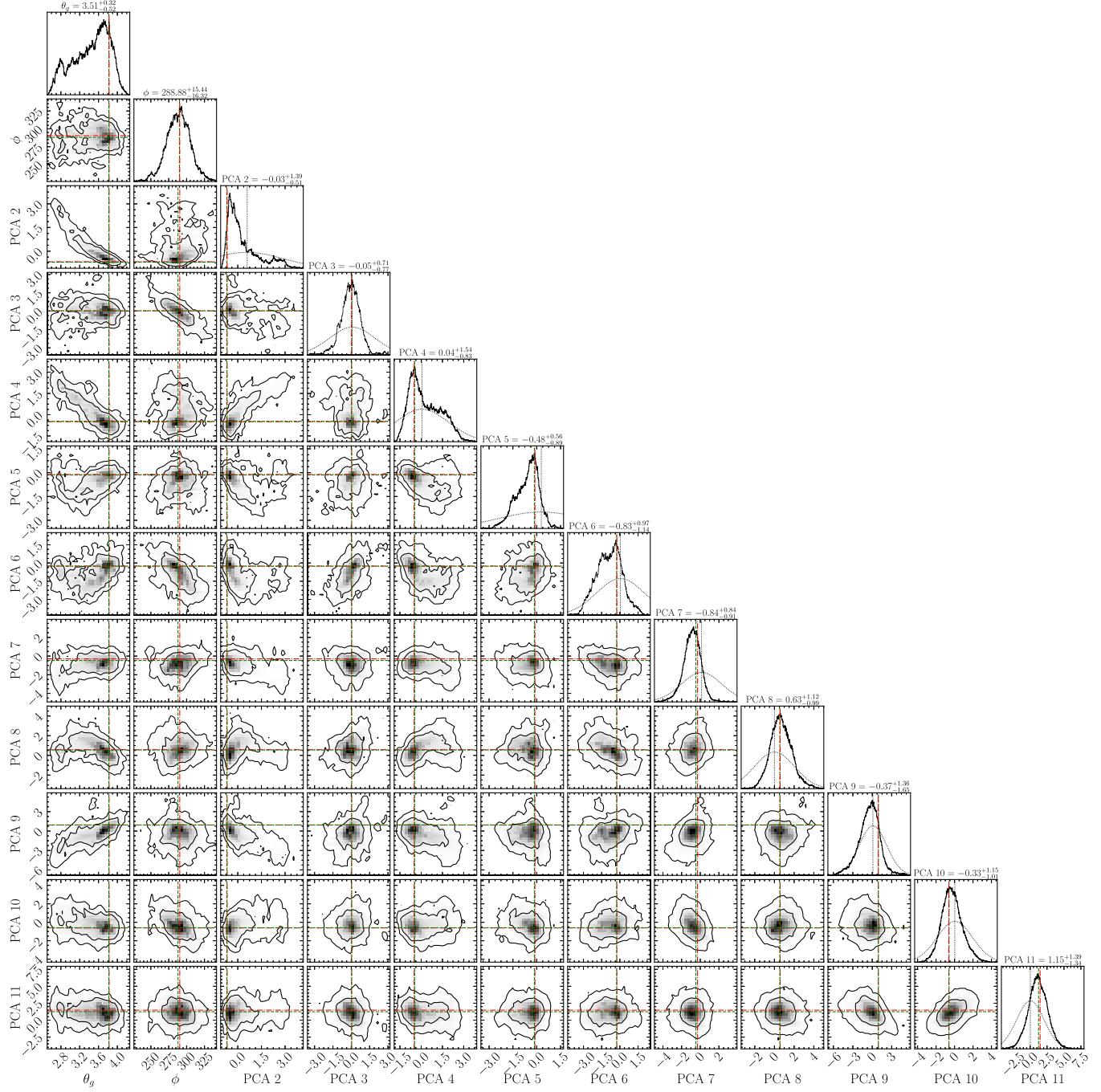


Figure 12. Corner plot for the MCMC run that corresponds to Figures 9, 10, and 11. Here, for brevity, we only include the flux parameter, the scaling parameter (θ_g), the orientation parameter (ϕ), and the amplitudes of the first 10 PCA components. The red vertical and horizontal dashed lines denote the values with the highest likelihood, while the vertical and horizontal green dashed lines denote the ground-truth values of these parameters. The dotted Gaussian curves and dotted vertical lines in the diagonal plots for the PCA amplitudes indicate the Gaussian prior for each amplitude used in the MCMC chain.

significant dip in visibility amplitude. The same reconstructions achieve a fractional error in visibility amplitude of less than $\sim 2\%$ and an error in visibility phase less than $\sim 15^\circ$ at all baselines less than $8\text{G}\lambda$. At baselines that do not coincide with the minima in visibility amplitude, the errors are significantly smaller; fractional complex error in visibility amplitude for reconstructions with just 20 PCA components is $\sim 2\%$ in regions between minima in visibility amplitude.

Since the reconstructions with only 20 PCA components achieve errors that are comparable to the errors in the EHT

2017 data for M87, in this work we settle on fitting 20 PCA components to synthetic data as a proof of concept. However, a slightly higher or lower number of components may achieve comparable or even better results. We use the results presented in Figure 8 to add a “theoretical error” to our model, which is implemented as an additional uncertainty, as a function of baseline length. In order to account for the fact that the peaks in the theoretical uncertainties shown in Figure 8 correspond to the locations of the visibility minima, which themselves scale inversely with θ_g , we scale the baseline lengths of the

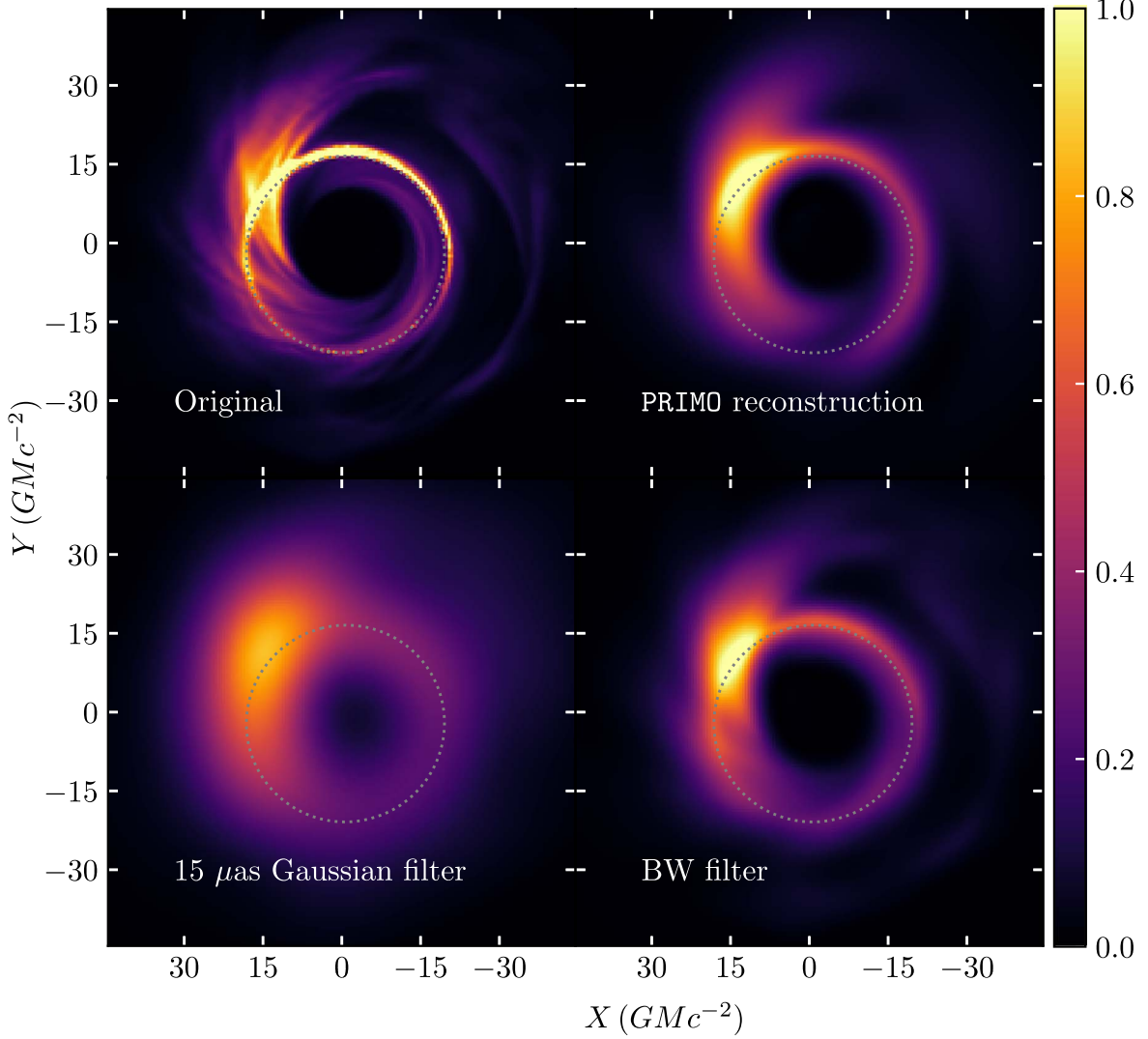


Figure 13. Same as Figure 9 but for the second synthetic data set we consider.

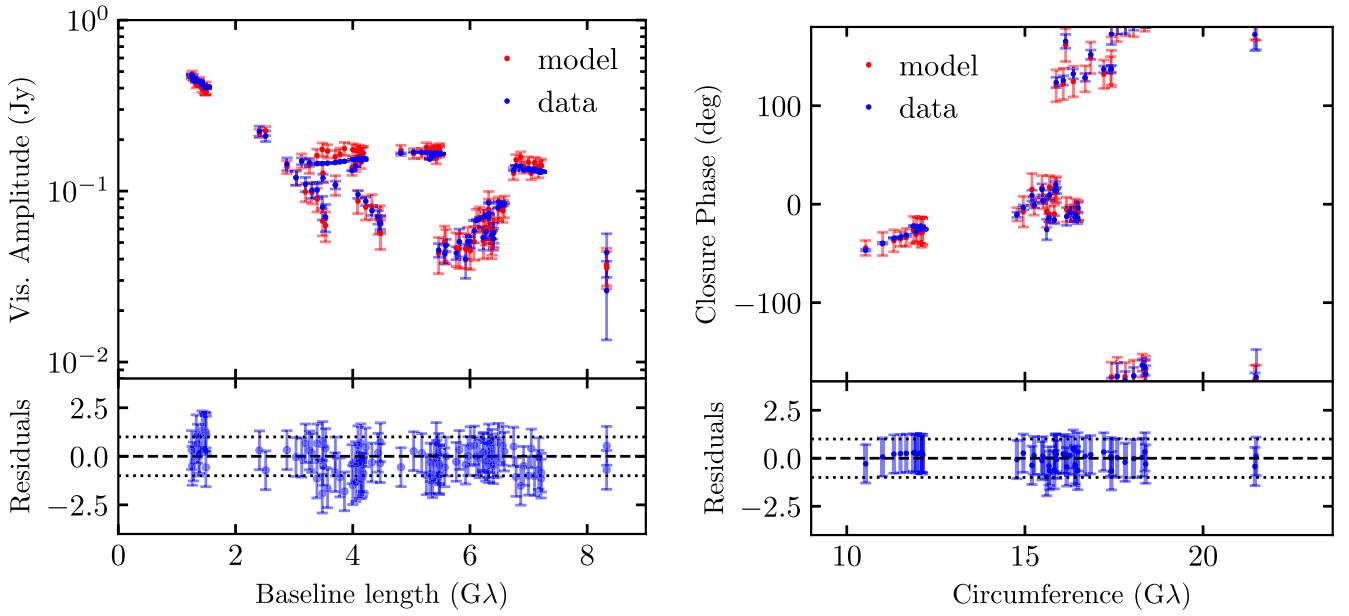


Figure 14. Same as Figure 10 but for the same synthetic data set as shown in Figure 13.

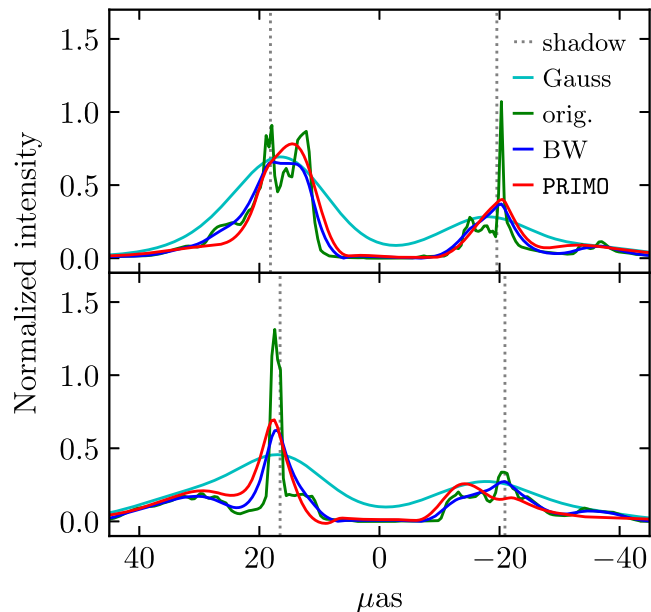


Figure 15. Same as Figure 11 but for the second synthetic data set.

theoretical error curves in a similar way. Moreover, because the errors shown in this figure are fractional, we multiply them by the total flux F in the image.

3.6. Preparing Simulated Data

The EHT observations are simulated as follows. For each data point in the M87 EHT data, we use sinc interpolation to interpolate between pixels in $u-v$ space and approximate the visibility at that $u-v$ location. In order to mimic thermal noise, we dither each data point with errors derived from a Gaussian distribution with a standard deviation set by the error in the EHT data at each $u-v$ location for the 2017 EHT observations of M87. We do not include gain errors in our synthetic data at this time, nor do we include gains as free parameters in our model.

4. Results from Synthetic Data

In order to demonstrate the performance of PRIMO with EHT data, we apply it to a number of synthetic data sets created from simulated snapshots. We start with two snapshots from a single GRMHD+radiative transfer MAD simulation with electron number density scale $n_e = 10^5 \text{ cm}^{-3}$, electron temperature parameter $R_{\text{high}} = 20$, black hole spin $a_{\text{BH}} = 0.9$, and mass $M = 6.5 \times 10^6 M_\odot$. This set of parameters is relevant to the black hole in M87 and is consistent with the recent EHT results that showed that the polarization structure of M87 shows preference to MAD models over SANE models (Event Horizon Telescope Collaboration et al. 2021a, 2021b). These two snapshots were also considered in Psaltis et al. (2022) but for different values of the R_{high} parameter.

We begin by applying our algorithm to a simulated image snapshot that resembles a crescent shape but has some extended structure. This snapshot was not easily fit by a simple geometric crescent model (Psaltis et al. 2022, see Figures 16 and 17). The top row of Figure 9 shows the simulated image and the highest likelihood reconstruction from PRIMO after 10,000,000 MCMC steps. Unlike the geometric crescent model, PRIMO can easily reproduce the morphology

of this image, arriving at the correct ring size and width, and the correct position angle for the peak of emission along the ring.

The bottom row of the figure shows the original image blurred by a Gaussian filter with a width of $15 \mu\text{as}$ and the original image after it was filtered with an $n = 2$, $r = 15 G\lambda$ Butterworth filter. The Gaussian-broadened image approximates previously published EHT images, since most of the EHT reconstructed images published to date have been broadened by Gaussians. The width of the Gaussian kernel was chosen such that the median FWHM of the image, along 128 equispaced radial cross sections emanating from the center of the black hole shadow, is equal to $20 \mu\text{as}$, i.e., similar to the M87 images reconstructed with other algorithms. (We note that we simply broadened the original simulated image and did not simulate CLEAN or regularized maximum likelihood (RML) imaging of it; still, the Gaussian-broadened GRMHD image provides a simplified comparison to the resolution of previously published EHT images.) PRIMO achieves much higher image fidelity than the Gaussian-blurred image and approaches the fidelity of the GRMHD input image simply blurred by the Butterworth filter.

Figure 10 compares the visibility amplitudes and the closure phases of the synthetic data created from the simulated image as described in Section 3.6 to those of the reconstructed image with the highest likelihood. The model shows very good agreement with the synthetic data and no structure is present in the residuals. As expected, because of the very large signal-to-noise ratio of most of the EHT measurements, the residuals are dominated by the theoretical errors introduced by the truncation in the number of PCA components used. Nevertheless, this truncation does not introduce any substantial biases in the image structure or its properties.

Figure 11 compares the vertical (N–S) and horizontal (E–W) cross sections of the original image, the Butterworth-filtered snapshot, the Gaussian-filtered snapshot, and the most likely reconstruction with PRIMO. There is remarkable agreement between the properties of the reconstructed image and those of the original one. In particular, the PRIMO fit is a much more accurate representation of the original snapshot than the snapshot convolved with a $20 \mu\text{as}$ beam. The main features of the cross sections, i.e., the location and amplitude of the peaks, the width of the peaks, the size and depth of the central flux depression, and the relative amplitude difference between the two peaks, are well approximated by the reconstruction.

Figure 12 shows a corner plot for numerous key parameters for the MCMC run discussed above. The corner plot shows a few correlations between parameters, such as between the scaling parameter θ_g and the amplitude of the second PCA component, as well as with several other components but to a lesser extent. Although the PCA components are orthogonal when considered across the entire image (or $u-v$ space), they are no longer orthogonal when we consider only the discrete locations of the EHT baselines. Because of this, some correlations between different PCA components are also visible, such as between the second and fourth components. The correlation between the overall scale (θ_g) and the second component is not surprising: the second component affects the width of the ring, which is highly correlated with the diameter of the ring.

The widths of the posteriors of most of the low-order PCA components are significantly smaller than those of the priors,

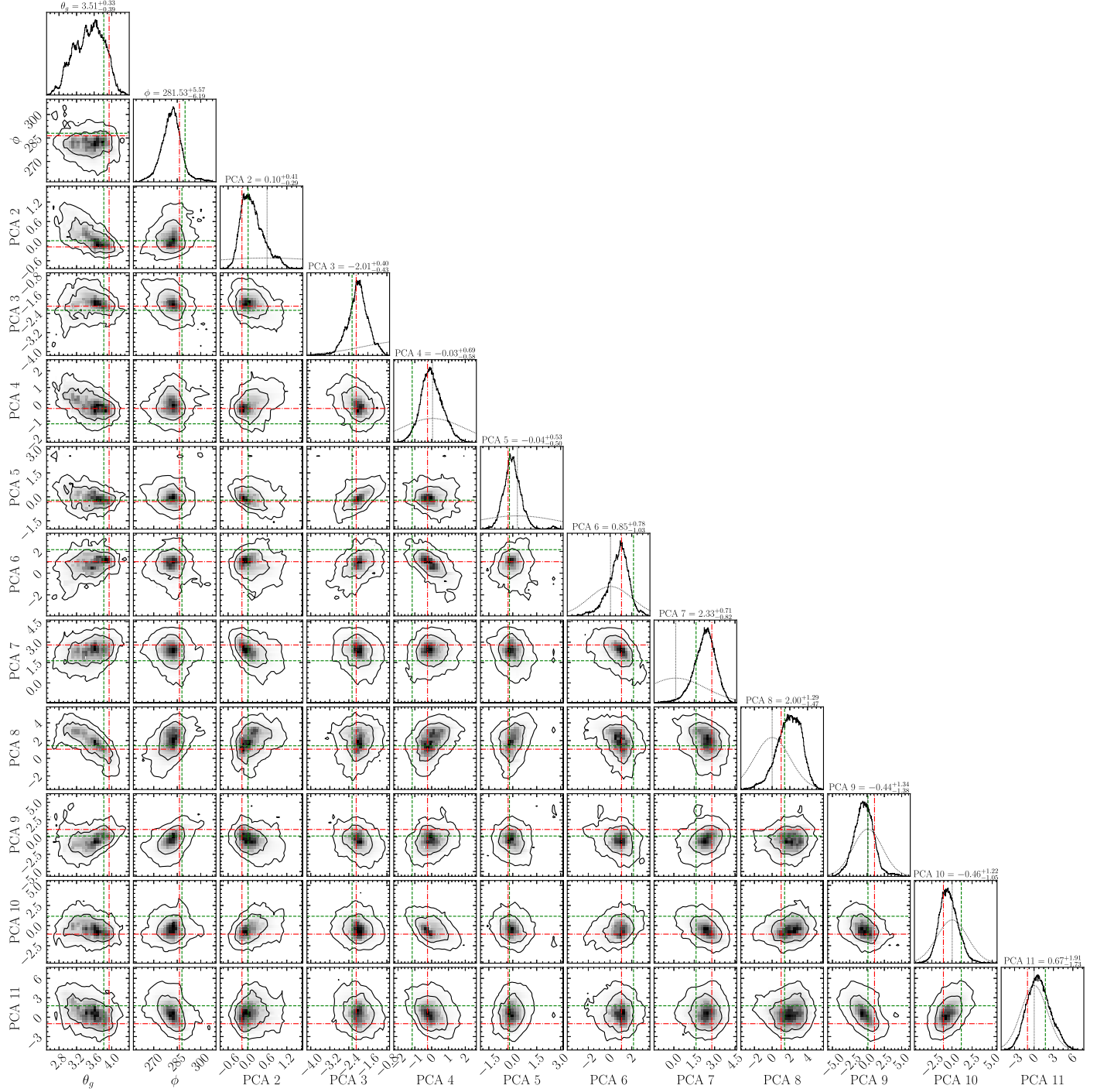


Figure 16. Same as Figure 12 but for the MCMC run shown in Figures 13, 14, and 15.

demonstrating that the broad-brush properties of the reconstructed image are driven by the data and not by the priors. This is increasingly less the case for the higher-order PCA components, justifying the level at which we truncated the series of components. The figure also compares the ground-truth values (shown in green) to the values with the highest likelihood from the reconstruction (shown in red).⁵ In all cases, there is a remarkable agreement between the two.

⁵ For the amplitudes of the PCA components, we treat the amplitudes derived by projecting the original image onto the first N PCA components as the ground-truth values.

As a second example, we apply PRIMO to synthetic data generated from a second snapshot that is dominated by an extended flux tube. The geometric crescent fit to this image failed to reconstruct a reasonable ring size even when a Gaussian component was added to the model (see Figures 18 and 19 in Psaltis et al. 2022). However, as can be seen in Figures 13–16, PRIMO can accurately reconstruct the location of the peak of emission along the ring, the width of the peak, the shape and depth of the central flux depression, and the extended flux tube toward the top left of the image. The visibility amplitudes and closure phases from the reconstructed

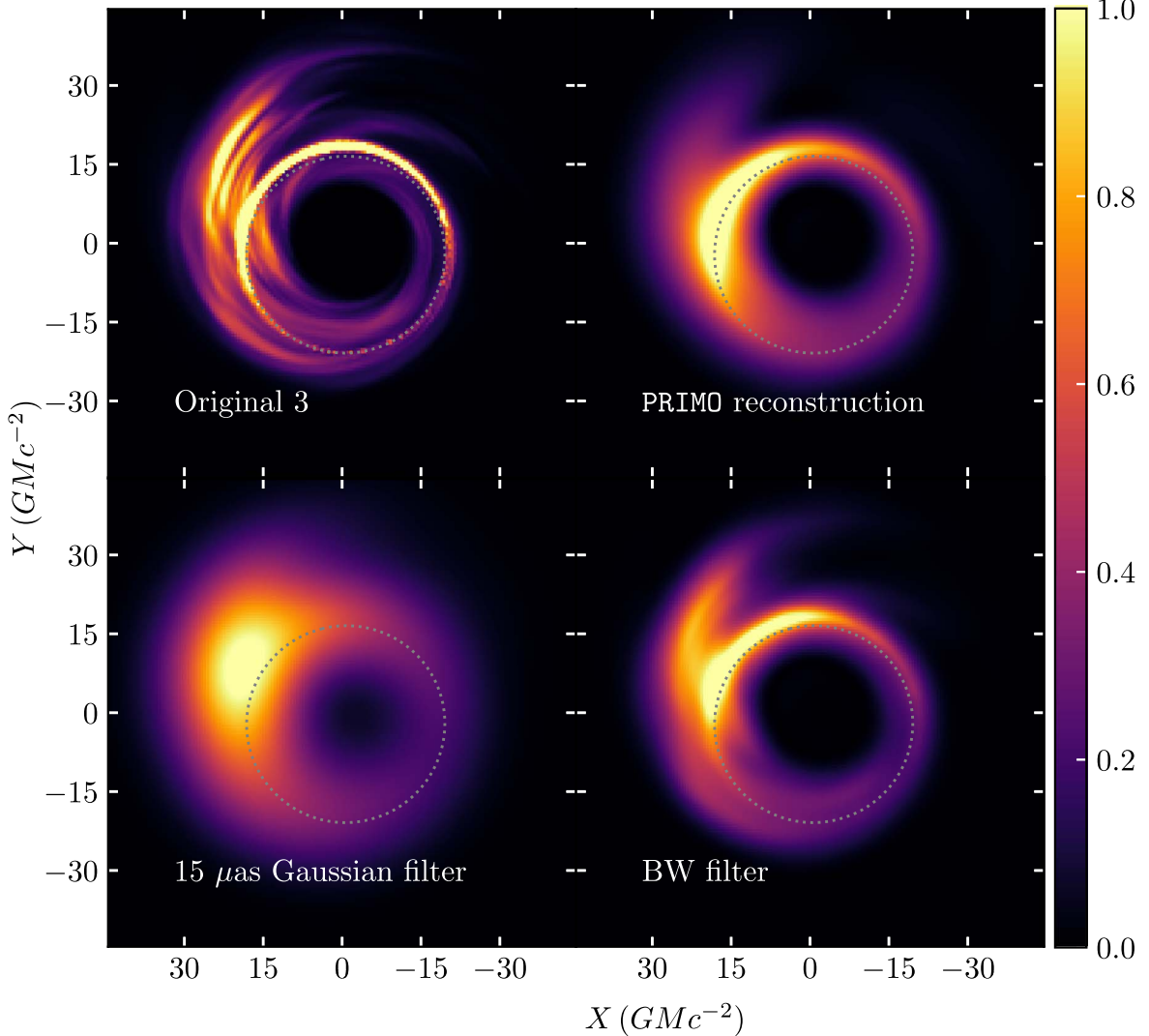


Figure 17. Same as Figure 9 but for the third synthetic data set, which was not contained in the training set but was generated from a GRMHD simulation with a SANE magnetic field geometry and a black hole spin of $a_{\text{BH}} = 0.7$. Despite not being part of the training set, salient features of the images are accurately reconstructed by PRIMO.

image show good agreement with the synthetic data and very little structure is visible in the residuals.

Finally, we consider an image that is not included in the training ensemble used to generate the PCA components. While all images in the training set have a black hole spin of $a_{\text{BH}} = 0.9$, for the final synthetic data set we use an image from a simulation with a black hole spin of $a_{\text{BH}} = 0.7$. This image has a SANE magnetic field geometry and a plasma parameter of $R_{\text{high}} = 20$. Figures 17, 18, and 19 show the results of reconstructing this image with PRIMO. Even though this image was not included in the ensemble used to generate the PCA components, the algorithm was still able to accurately reconstruct the salient image features, such as the depth and shape of the brightness depression, the size and width of the peak, the orientation of the peak brightness asymmetry in the ring feature, and the extended structure toward the top left of the image.

5. Summary

We have presented a novel PCA-based image reconstruction algorithm, PRIMO, for reconstruction of black hole images

from EHT data. Our algorithm is unique in that it combines prior information from physically motivated simulations to reconstruct images that lie in the same general space of images spanned by the simulations. Each simulation can create countless images with different morphologies due to the turbulent nature of the accretion flow, making it unlikely that the particular realization of the turbulent flow of the source that the EHT observes would be well fit by any one of the thousands of simulation images included in our library. However, the PCA-based algorithm allows us to reconstruct images regardless of whether or not they are contained within the library of images from which the PCA basis was created. Compared to the results of previous work, PRIMO is not severely affected by the biases identified in Psaltis et al. (2022), where simulated images were fit with analytic crescent models.

Throughout this work we have used the EHT baseline coverage from the 2017 observations. Since then, the EHT has observed several more times with additional telescopes. We expect that, with additional baselines, we will be able to incorporate a higher number of PCA components to generate images from the data and achieve even better angular

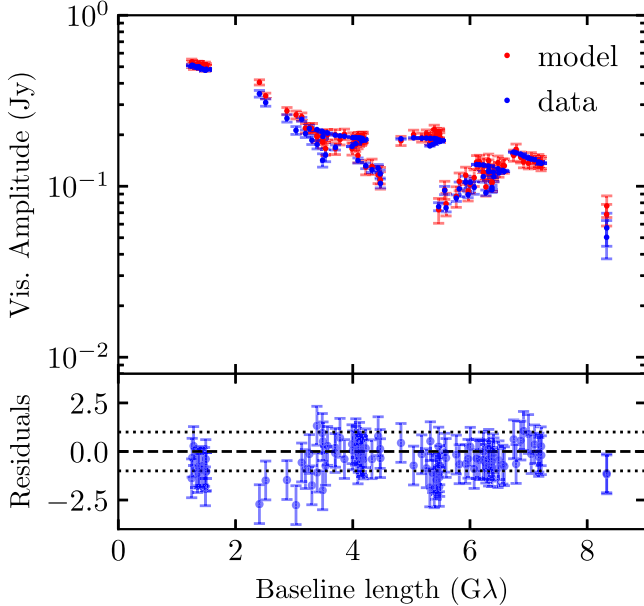


Figure 18. Same as Figure 9 but for the third synthetic data set we consider.

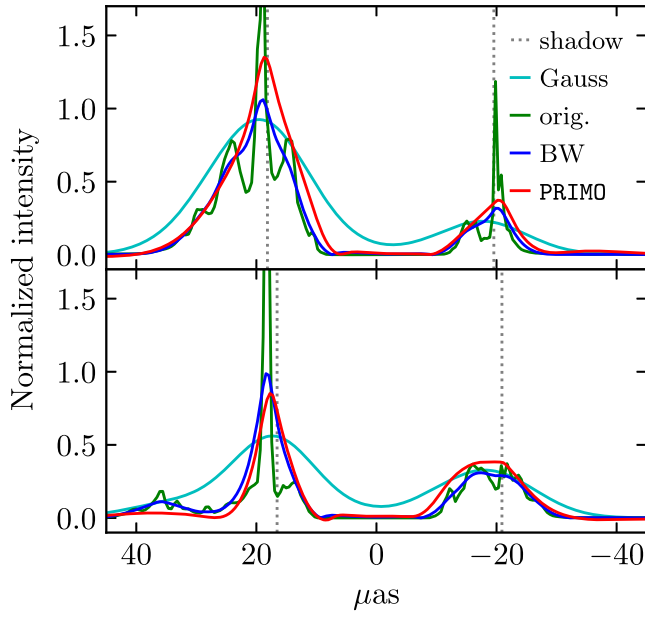
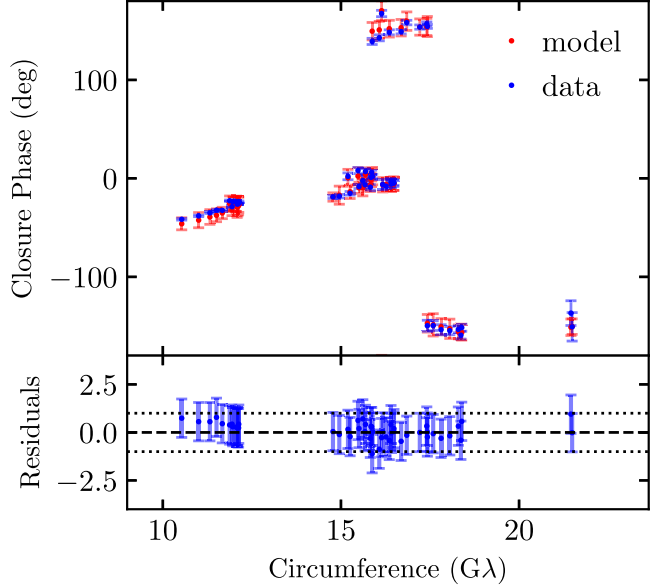


Figure 19. Same as Figure 11 but for the third synthetic data set we consider.

resolution. The EHT is also planning to observe at 345 GHz in the coming years, which will allow us to probe even higher spatial frequencies. PRIMO can easily be adapted to exploit these new observations.

We thank C. K. Chan, P. Hallur, and B. Zackay for useful discussions. L. M. gratefully acknowledges support from an NSF Astronomy and Astrophysics Postdoctoral Fellowship under award no. AST-1903847. D.P. and F.O. gratefully acknowledge support from NSF PIRE grant 1743747 for this work. All ray-tracing calculations were performed with the El Gato GPU cluster at the University of Arizona that is funded by NSF award 1228509.



ORCID iDs

- Lia Medeiros <https://orcid.org/0000-0003-2342-6728>
- Dimitrios Psaltis <https://orcid.org/0000-0003-1035-3240>
- Tod R. Lauer <https://orcid.org/0000-0003-3234-7247>
- Feryal Özel <https://orcid.org/0000-0003-4413-1523>

References

- Akiyama, K., Ikeda, S., Pleau, M., et al. 2017, *AJ*, 153, 159
- Blackburn, L., Chan, C.-k., Crew, G. B., et al. 2019, *ApJ*, 882, 23
- Bracewell, R. N. 1986, *The Fourier Transform and Its Applications* (New York: McGraw-Hill)
- Butterworth, S. 1930, *Wireless Engineer*, 7, 536
- Chael, A. A., Johnson, M. D., Narayan, R., et al. 2016, *ApJ*, 829, 11
- Chan, C.-k., Psaltis, D., & Özel, F. 2013, *ApJ*, 777, 13
- Chan, C.-k., Psaltis, D., Özel, F., et al. 2015a, *ApJ*, 812, 103
- Chan, C.-K., Psaltis, D., Özel, F., Narayan, R., & Sadowski, A. 2015b, *ApJ*, 799, 1
- Event Horizon Telescope Collaboration, Akiyama, K., Alberdi, A., et al. 2019a, *ApJL*, 875, L1
- Event Horizon Telescope Collaboration, Akiyama, K., Alberdi, A., et al. 2019b, *ApJL*, 875, L2
- Event Horizon Telescope Collaboration, Akiyama, K., Alberdi, A., et al. 2019c, *ApJL*, 875, L3
- Event Horizon Telescope Collaboration, Akiyama, K., Alberdi, A., et al. 2019d, *ApJL*, 875, L4
- Event Horizon Telescope Collaboration, Akiyama, K., Alberdi, A., et al. 2019e, *ApJL*, 875, L5
- Event Horizon Telescope Collaboration, Akiyama, K., Alberdi, A., et al. 2019f, *ApJL*, 875, L6
- Event Horizon Telescope Collaboration, Akiyama, K., Algaba, J. C., et al. 2021a, *ApJL*, 910, L12
- Event Horizon Telescope Collaboration, Akiyama, K., Alberdi, A., et al. 2021b, *ApJL*, 910, L13
- Gammie, C. F., McKinney, J. C., & Tóth, G. 2003, *ApJ*, 589, 444
- Gebhardt, K., Adams, J., Richstone, D., et al. 2011, *ApJ*, 729, 119
- Gheller, C., & Vazza, F. 2022, *MNRAS*, 509, 990
- Högbom, J. A. 1974, *A&AS*, 15, 417
- Igumenshchev, I. V., Narayan, R., & Abramowicz, M. A. 2003, *ApJ*, 592, 1042
- Kamruddin, A. B., & Dexter, J. 2013, *MNRAS*, 434, 765
- Kim, J., Marrone, D. P., Chan, C.-K., et al. 2016, *ApJ*, 832, 156
- Mardia, K. V., & Jupp, P. E. 2009, *Directional Statistics*, Vol. 494 (Chichester: Wiley)
- Medeiros, L., Chan, C.-K., Narayan, R., Özel, F., & Psaltis, D. 2022, *ApJ*, 924, 46
- Medeiros, L., Chan, C.-k., Özel, F., et al. 2017, *ApJ*, 844, 35

- Medeiros, L., Chan, C.-k., Özel, F., et al. 2018a, *ApJ*, **856**, 163
 Medeiros, L., Lauer, T. R., Psaltis, D., & Özel, F. 2018b, *ApJ*, **864**, 7
 Medeiros, L., Psaltis, D., & Özel, F. 2020, *ApJ*, **896**, 7
 Mościbrodzka, M., Falcke, H., & Shiokawa, H. 2016, *A&A*, **586**, A38
 Narayan, R., Sadowski, A., Penna, R. F., & Kulkarni, A. K. 2012, *MNRAS*, **426**, 3241
 Psaltis, D., Medeiros, L., Lauer, T. R., Chan, C.-K., & Özel, F. 2020, arXiv:2004.06210
 Psaltis, D., Özel, F., Chan, C.-K., & Marrone, D. P. 2015, *ApJ*, **814**, 115
 Psaltis, D., Özel, F., Medeiros, L., et al. 2022, *ApJ*, **928**, 55
 Ressler, S. M., Tchekhovskoy, A., Quataert, E., Chandra, M., & Gammie, C. F. 2015, *MNRAS*, **454**, 1848
 Satapathy, K., Psaltis, D., Özel, F., et al. 2022, *ApJ*, **925**, 13
 Shao, L., Yan, R., Li, X., & Liu, Y. 2014, *IEEE Trans. Cybernetics*, **44**, 1001
 Sadowski, A., Narayan, R., Penna, R., & Zhu, Y. 2013, *MNRAS*, **436**, 3856
 Turk, M., & Pentland, A. 1991, *J. Cognitive Neurosci.*, **3**, 71
 Walker, R. C., Hardee, P. E., Davies, F. B., Ly, C., & Junor, W. 2018, *ApJ*, **855**, 128
 Walsh, J. L., Barth, A. J., Ho, L. C., & Sarzi, M. 2013, *ApJ*, **770**, 86
 Zhu, G. 2016, arXiv:1612.06037